J. Fluid Mech. (2021), *vol*. 908, A39. © The Author(s), 2020.
Published by Cambridge University Press
doi:10.1017/jfm.2020.934

Particle–fluid–wall interaction of inertial spherical particles in a turbulent boundary layer

Lucia J. Baker[1,2,†] **and Filippo Coletti**[1,2,‡]

[1]Department of Aerospace Engineering and Mechanics, University of Minnesota, Minneapolis, MN 55455, USA

[2]St. Anthony Falls Laboratory, University of Minnesota, Minneapolis, MN 55414, USA

(Received 2 May 2020; revised 6 September 2020; accepted 17 October 2020)

We study the dynamics of dilute, slightly negatively buoyant, millimetre-size spherical particles fully suspended in a smooth-wall open channel flow. The Reynolds number is $Re_\tau = 570$ and the particle Stokes number is $St^+ = 15$. Particle image velocimetry and tracking are used to obtain simultaneous, time-resolved flow fields and particle trajectories. Particles travel at a lower mean velocity than the fluid: in the log layer this is due to the oversampling of slow fluid regions, but closer to the wall the cause is instantaneous slip between particles and fluid. The particle Reynolds stresses exceed those of the fluid. Near the wall, the particle streamwise diffusivity is larger than the momentum diffusivity, while the opposite is true for the wall-normal component. The particle transport is strongly linked to ejections, while the role of sweeps is marginal, and there is no evidence of turbophoresis. The concentration profile follows a power law with a shallower slope than predicted by equilibrium theories that neglect particle inertia. Upward-/downward-moving particles display positive/negative mean streamwise acceleration due to the particle–fluid slip. The particles that contact the wall are faster than the local fluid both before reaching the wall and after leaving it. Therefore, they are decelerated by drag and pushed downward by shear-induced lift. The durations of wall contact follow exponential distributions with characteristic time scale close to the particle response time. Lift-offs coincide with particles meeting a fluid ejection. These observations emphasize the competing effects of inertia and gravity.

Key words: sediment transport, particle/fluid flow, turbulent boundary layers

1. Introduction

Describing and predicting the behaviour of inertial particles in turbulent boundary layers has been a major goal in fluid dynamics since the work of Shields (1936), Bagnold (1936), Rouse (1937) and Prandtl (1952), who first began quantifying the transport of sediment in air and water flows. The experiments of Shields (1936) revealed a relationship predicting the initiation of motion of the sediment from the particle inertia and the fluid shear stress on the wall. Bagnold (1936) observed the saltation of sand grains in air and developed an empirical relationship quantifying their flux as a function of the

† Email address for correspondence: bake0616@umn.edu
‡ Present address: Department of Mechanical and Process Engineering, ETH Zurich, Switzerland.

fluid flow parameters. Rouse (1937) analytically derived an expected concentration profile of suspended sediment as a function of wall-normal height, under equilibrium between turbulent resuspension and gravitational settling. Under the same assumption, Prandtl (1952) used a linear diffusivity model to derive a parabolic concentration profile which is still the *de facto* standard. These models are effective at describing the observed bulk transport properties but do little to shed light on the underlying physical mechanisms at the particle scale.

More recently, thanks to non-intrusive measurement techniques, several researchers used detailed experiments to further understand the interaction between the inertial particles and the wall turbulence. Due to its relevance to sediment transport in water bodies, many studies in the geophysical research literature focused on the case in which the suspension is eroded from and deposited to a bed of particles. For example, Hurther & Lemmin (2003) investigated the transport of suspended particles in a turbulent open channel flow by comparing statistics of particle mass flux with turbulent momentum flux and concluded that coherent structures are a dominant mechanism of particle transport. Lajeunesse, Malverti & Charru (2010) used imaging to investigate the relation between the flow turbulence and the intermittent motions of the particles alternating rest and flight. Heyman, Bohorquez & Ancey (2016) empirically determined closure equations for particle bed load transport in terms of known flow conditions, such as particle diffusivity and suspension/deposition rates.

The presence of a changing wall roughness and the mobilization of a polydisperse bed complicate the task of isolating the particle–fluid dynamics. Somewhat surprisingly, the smooth-wall case has been considered in a limited number of experimental studies. Kaftori, Hetsroni & Banerjee (1995*a*) measured velocity and concentration profiles of sub-millimetre polystyrene particles in a horizontal water flume and found that particles preferentially concentrate in regions of low fluid velocity associated with near-wall streaks. Niño & Garcia (1996) confirmed that particles in a smooth-wall flume arranged themselves in long streaks generated by streamwise vortices in the inner layer. Tanière, Oesterlé & Monnier (1997) looked at solid particles in a wind tunnel and reported large fluctuations of the dispersed phase velocity, attributing them to saltation at the wall. Kiger & Pan (2002) found evidence that particles congregate in specific structures in the turbulent boundary layer, and showed a difference between ascending and descending particles: upward-moving particles were concentrated in ejections (events with negative streamwise fluctuation and positive wall-normal fluctuation of the fluid velocity); whereas downward-moving particles showed a weaker association with sweeps (events with positive streamwise fluctuation and negative wall-normal fluctuation). This was later confirmed by detailed time-resolved measurements, e.g. van Hout (2011, 2013) and Rabencov, Arca & van Hout (2014). Righetti & Romano (2004) studied glass particles in water at a volume fraction of 10^{-3} and observed significant modulation of the fluid turbulence, which they attributed to the inter-phase momentum exchange during entrainment from and deposition to the wall. Gerashchenko *et al.* (2008) measured the acceleration of inertial particles in a turbulent boundary layer and found that acceleration variance increased with particle inertia, contrary to what happens in isotropic turbulence (Bec *et al.* 2006). Ebrahimian, Sanders & Ghaemi (2019) investigated in detail the particle acceleration and its relation to turbulent events and showed that particles may slide along the wall for considerable time. Tee, Barros & Longmire (2020) performed detailed, three-dimensional measurements on a single large spherical particle interacting with the wall in a turbulent boundary layer and found that spheres underwent minimal rotation while lifting off the wall, and that spanwise forces on the particles can be important. Berk & Coletti (2020) considered microscopic glass beads in a wind tunnel. They highlighted

how the particle inertia is responsible for discrepancies from the concentration profile predicted by the Rouse–Prandtl theory (Rouse 1937; Prandtl 1952), and investigated the roots of the relative particle–fluid velocity. Due to the limited accuracy in locating the small particles, they could not measure the settling velocity, which is known to be strongly altered by turbulence (Nielsen 1993; Wang & Maxey 1993; Sabban & van Hout 2011; Petersen, Baker & Coletti 2019).

The numerical studies of inertial particles in smooth-wall turbulence have been much more numerous and have allowed in-depth analysis of the problem, especially using direct numerical simulation of the fluid flow coupled with advection of point particles, e.g. Rouson & Eaton (2001), Marchioli & Soldati (2002), Zhao, Andersson & Gillissen (2010), Zamansky, Vinkovic & Gorokhovski (2011), Sardina *et al.* (2012), Bernardini (2014), Richter & Sullivan (2014) and Lee & Lee (2015). Typically, a simplified version of the particle transport equation was used, which is only valid in the limit of vanishingly small particle Reynolds number (Maxey & Riley 1983). Also, in the majority of these cases (included the ones mentioned above) gravity was neglected; this isolates the effect of particle inertia but prevents the direct application of the results to practical settings. The few studies that considered wall-normal gravity (among others, Lavezzo *et al.* 2010; Lee & Lee 2019) underscored its importance and interplay with the mean shear. In particular, Lee & Lee (2019) indicated that gravity greatly reduced turbophoresis, i.e. the tendency of the particles to drift down the gradient of Reynolds stresses (hence towards the wall) due to the interaction with streamwise vortices (Marchioli & Soldati 2002).

The limitations of the point-particle approach may be exacerbated in particle-laden turbulent boundary layers where wall-normal gravity is important: the assumption of negligible particle-size effects is particularly limiting near the wall, where the flow scales are the smallest and the number density the highest. Forces which are normally considered negligible for microscopic particles (e.g. added mass, Saffman and Magnus lift; see Crowe *et al.* 2011) may be important, and advanced methods are especially needed to account for the flow distortion by the particles. While effective point-particle strategies to address the latter issue have recently been proposed (Capecelatro & Desjardins 2013; Gualtieri *et al.* 2015; Horwitz & Mani 2016; Ireland & Desjardins 2017; Balachandar, Liu & Lakhote 2019), numerical advances and ever-growing computational resources have enabled particle-resolved direct numerical simulations (Kidanemariam *et al.* 2013; Picano, Breugem & Brandt 2015; Lin *et al.* 2017; Wang, Abbas & Climent 2017). Still, these studies are mostly limited to small Reynolds numbers and relatively large particles. Importantly, it is hard to validate these simulations against the scarce experimental studies focused on the detailed particle–wall–fluid dynamics, especially considering that most of the experimental literature is concerned with geophysical flows including particle polydispersity, bed roughness and mobile beds.

Here, we consider the fundamental case of highly dilute, mono-dispersed, spherical particles suspended by a turbulent boundary layer over a horizontal smooth wall, where particles interact with the wall but do not deposit on it. We perform laboratory experiments and leverage simultaneous time-resolved imaging of both phases to explore the details of the particle–fluid interaction across the boundary layer. The organization of the paper is as follows: the experimental methods, facility, and image processing are described in § 2; in § 3 we report on the fluid and particle velocity (§ 3.1), particle slip velocity (§ 3.2), Reynolds stresses of both phases (§ 3.3), correlation of particle and fluid fluctuations (§ 3.4), particle diffusivity (§ 3.5), concentration and flux profiles (§ 3.6), acceleration (§ 3.7) and interaction with the wall (§ 3.8); the conclusions are summarized in § 4.

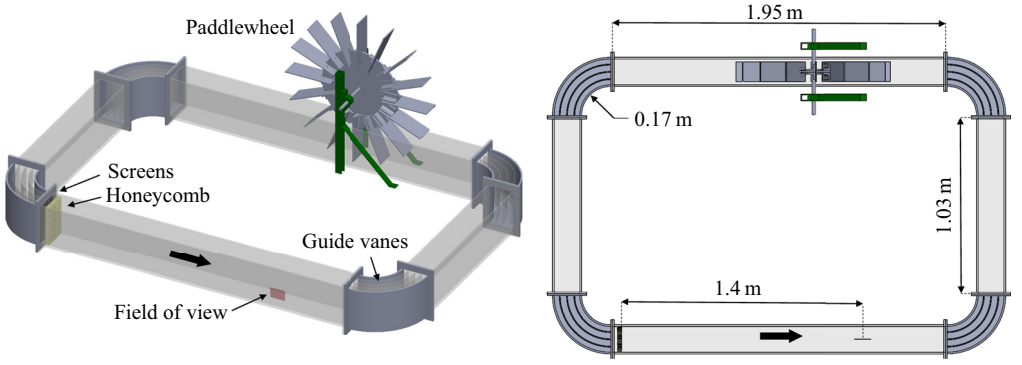

FIGURE 1. Diagram of the water channel showing key components and dimensions. The bold arrow indicates the direction of the flow.

2. Experimental method

2.1. *Experimental facility*

A recirculating open channel with water as the working fluid is used for this experiment. Complete details of the channel design and its performance to produce fully developed turbulent boundary layers can be found in Adhikari (2013) and Baker & Coletti (2019) and are just summarized here. The channel walls and floor are made of transparent acrylic. The channel width is 15 cm, with the water filled to a depth $H = 15$ cm. Guide vanes are placed in each of the four corners to reduce secondary flows produced at the turns. The test section is located 1.4 m downstream of a corner, allowing the flow to reach a developed state, which was verified by comparing fluid velocity statistics from the upstream and downstream ends of the test section. A diagram of the channel is shown in figure 1. The flow is provided by a paddlewheel with 16 paddles driven by a 1/4 HP permanent magnet motor (Leeson, USA) at a constant angular speed of 10 revolutions per minute. This is used instead of a centrifugal pump to avoid damaging the particles and the pump. The resulting free-stream velocity is 0.42 m s^{-1}, which is measured to be constant in time within experimental uncertainty. Two wire screens with a grid spacing of 4 mm and one honeycomb with a cell size of 7 mm and a depth of 25 mm are placed upstream of the test section, as shown in figure 1.

2.2. *Particles*

Spherical polystyrene (PS) particles (Composition Materials Co., USA) are used. The particles are transparent, but their index of refraction causes significant scattering of the illumination light, and they appear as shown in figure 2. Because polystyrene is hydrophobic, the particles are first mixed in a dilute solution of water and a surfactant (dish soap) before introducing them into the channel to allow them to disperse.

The physical properties of the particles are listed in table 1. The diameter D_p is measured by imaging about 230 particles placed on a tray in a single layer. Their detection and sizing are performed via a circle-finding function based on the Hough transform. The probability density function (PDF) of the particle diameters is plotted in figure 3. For completeness, we also report the value of the Galileo number $Ga = [(\rho_p/\rho_f - 1)gD_p^3/\nu^2]^{1/2}$ and the Shields number $Sh = u_\tau^2/[(\rho_p/\rho_f - 1)gD_p]$, where ρ_p is the particle density, ρ_f is the fluid density, g is gravitational acceleration, ν is the fluid kinematic viscosity and u_τ is the friction velocity (defined in § 3.1). These indicate that the effect of gravity is significant (as

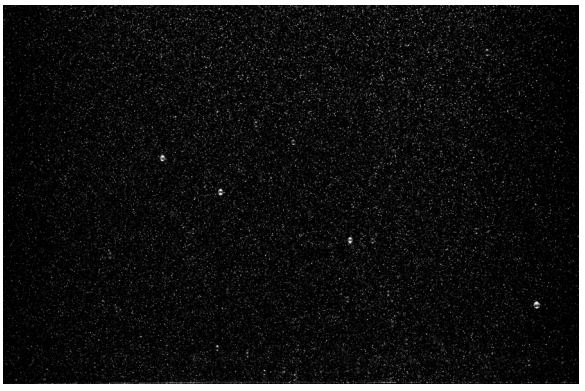

FIGURE 2. Instantaneous realization of the particle-laden flow. Both the mm-sized spherical PS particles and the microscopic silver-coated glass tracer particles are visible.

D_p (mm)	D_p^+	ρ_p (kg m^{-2})	V_t (mm s^{-1})	V_t/u_τ	Re_{p,V_t}	τ_p (ms)	St^+	Ga	Sh	Φ_v
0.83	16	1018.6	13.9	0.75	13	43.3	15	11.3	2.0	10^{-4}

TABLE 1. Properties of the PS particles; D_p is the mean particle diameter, D_p^+ is the diameter normalized by the viscous length scale of the flow, ρ_p is the density, V_t is the terminal velocity in still water, Re_{p,V_t} is the Reynolds number based on V_t, τ_p is the particle response time, St^+ is the particle Stokes number based on the viscous time scale of the flow, Ga is the Galileo number, Sh is the Shields number and Φ_v is the particle volume fraction.

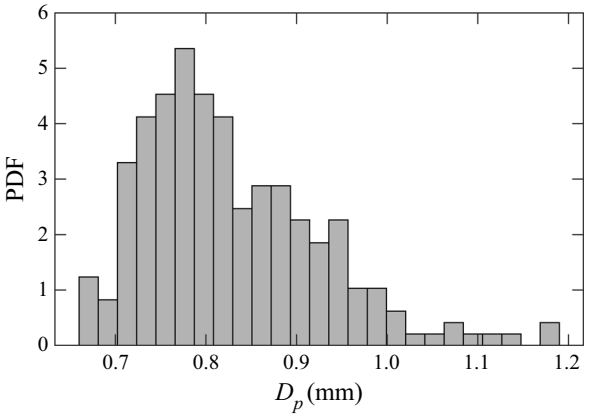

FIGURE 3. Probability density function of PS particle diameters. The standard deviation is 12 % of the mean value.

also indicated by the ratio V_t/u_τ, of order one), although the particles are in a continuous transport (full suspension) regime.

The terminal velocity V_t is measured by dropping individual particles from rest in a large tank of quiescent water and recording 60 frame-per-second videos. Particles are tracked using the same method used for the particle-laden flow measurements, which will

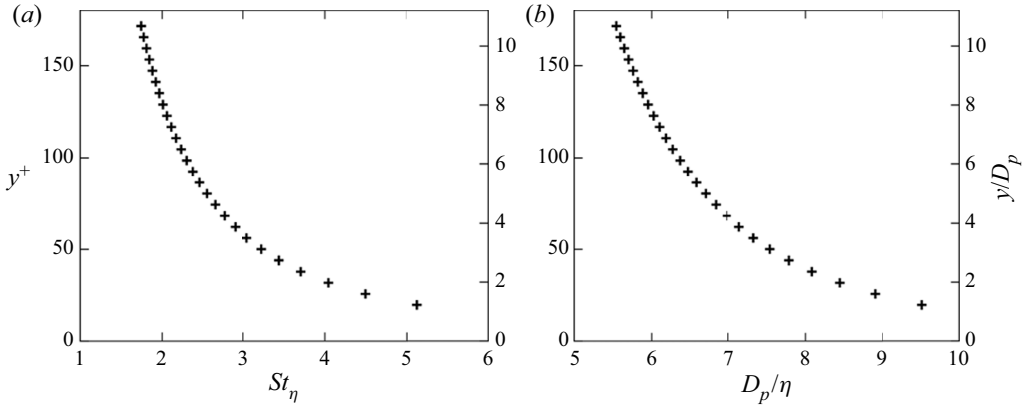

FIGURE 4. Wall-normal profiles of (*a*) the particle Stokes number based on the Kolmogorov scale and (*b*) the particle diameter normalized by the Kolmogorov scale.

be described in the next section. The tank is deep enough (0.3 m) for the particles to reach a steady-state velocity before touching the bottom. The nominal particle Reynolds number is computed based on the terminal velocity, $Re_{p,V_t} = \rho_f V_t D_p/\mu$, where ρ_f and $\mu = \rho_f \nu$ are the water density and dynamic viscosity, respectively. This Reynolds number is used to correct the Stokes drag coefficient according to the Schiller & Naumann correction (Clift, Grace & Weber 2005), which in turn is used to estimate the particle density ρ_p from the measured terminal velocity.

To quantify particle inertia, we refer to the Stokes number, i.e. the ratio between the particle response time and a relevant fluid time scale. As for the particle response time, we consider the characteristic time scale with which the particle exponentially approaches the steady-state velocity of the surrounding fluid, $\tau_p = \rho_p D_p^2/(18\mu)$. We favour this definition over the other commonly used response time, $(\rho_p - \rho_f)D_p^2/(18\mu)$, which describes the exponential approach to terminal velocity of a particle settling in a still fluid. As for the fluid, both the viscous time scale τ^+ and the Kolmogorov time scale τ_η are relevant; τ^+ is based on the friction velocity u_τ, estimated from fitting the log law to the measured velocity profile (see § 3.1), from which we define $St^+ = \tau_p/\tau^+$ (the superscript '+' denoting, here and in the following, normalization by wall units). The value of τ_η varies with the wall-normal distance and is estimated from the production–dissipation balance in the turbulent boundary layer (Pope 2000). This gives a range for the Stokes number $St_\eta = \tau_p/\tau_\eta$ and for the ratio of particle diameter to Kolmogorov length D_p/η, both reported in figure 4.

The volume fraction of the particles in the system, Φ_v, is approximately 10^{-4}. Thus, at the present particle-to-fluid density ratio, the momentum two-way coupling effects are expected to be localized and have a minimal impact on the fluid statistics. This is verified in § 3.1 by showing that the unladen and laden fluid velocity profiles overlap within experimental uncertainty.

2.3. *Fluid velocity measurements*

Time-resolved planar particle image velocimetry (PIV) is used to measure the velocity of the fluid. The water is seeded with 13 micron silver-coated glass bubbles (Potters Industries) to act as tracers. A 300 W near-infrared pulsed laser with a wavelength of 808 nm (Oxford Lasers, Firefly 300W) is used for illumination. The laser is positioned

f_s (Hz)	N	w (mm)	h (mm)	w_i (mm, wall units)	δx (mm, wall units)
500	65 700	95	63	1.26, 24.3^+	0.31, 6.1^+

TABLE 2. Imaging and PIV processing parameters: f_s is the imaging frequency; N is the number of images; w and h are the field of view width and height, respectively; w_i is the final-pass PIV interrogation window size; and δx is the PIV vector spacing.

above the channel and emits a 1 mm light sheet perpendicular to the floor and parallel to the streamwise direction, illuminating the channel symmetry plane. A 15 cm square acrylic plate is fixed at the water surface to avoid distortion of the laser sheet. This results a in shear layer below the plate less than 1 cm deep, which does not affect our region of interest. Images are captured with a high-speed, 4-megapixel CMOS camera (Phantom VEO 640L) viewing through one of the sidewalls. The camera mounts a 105 mm lens, capturing the bottom 6 cm of the channel. For optimal tracking, the frame rate is chosen to obtain typical displacements of about one particle diameter (approximately 20 pixels). The recording time amounts to approximately 1900 boundary-layer turnover times.

The image processing routine is similar to what is described in Petersen *et al.* (2019). First the PS particles are identified (using the method described in § 2.4) and substituted with Gaussian noise having the same mean and standard deviation as the background image. The resulting tracer-only images are used for PIV processing performed with a custom-written software. A minimum-intensity background subtraction is then performed which removes consistent bright spots caused by reflections and glare off the wall. Multi-pass cross-correlation with an overlap of 75 % between interrogation windows is used to compute fluid displacement fields. Initial, intermediate and final interrogation window sizes of 128^2, 64^2 and 32^2 pixels are used, respectively. A signal-to-noise ratio criterion and a universal outlier detection (Westerweel & Scarano 2005) are used to reject spurious velocity vectors. The imaging and PIV processing parameters are summarized in table 2.

2.4. *Particle detection and tracking*

To locate the particles, a convolution method using a particle template image is used, similar to van Hout, Sabban & Cohen (2013) (figure 5). First, a low-pass median filter with a width of nine pixels is applied to the original images (figure 5*a*) to remove the tracers (figure 5*b*). Then, images are convolved with a particle template image (figure 5*c*). The particle centroids are then identified as convolution peaks which surpass a specified threshold (figure 5*d*), whose exact value is verified to have negligible impact on the results.

The centroids are tracked between successive image pairs using a PIV-based predictor: a first-guess displacement is estimated from the mean fluid velocity profile interpolated at the wall-normal location of each particle centroid and subtracted from the second frame in the pair. Then, a nearest-neighbour search with a search radius of one particle diameter is used to match particle centroids in the first frame with the shifted centroids in the second one. As the inter-frame particle displacement is about one particle diameter, there is no ambiguity in matching particle images. Approximately 2400 particles were tracked within the image set. In the data analysis, we will consider the fluid velocity at the particle location, $u_{f|p}$. This is obtained by interpolating the PIV vectors onto the instantaneous particle centroid location using an inverse-distance-weighted average of the fluid velocity

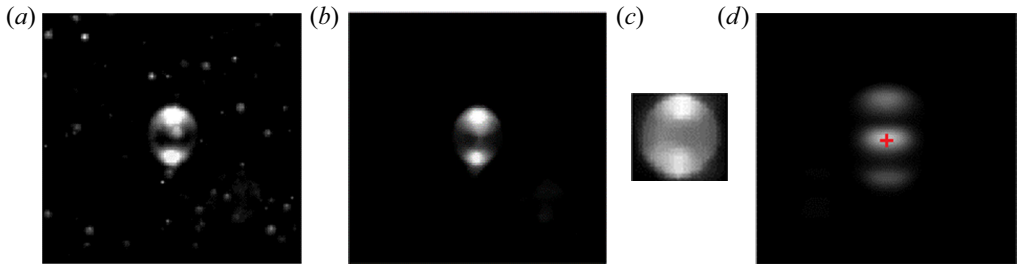

FIGURE 5. Convolution method for particle detection: (*a*) original image, (*b*) median filtered image, (*c*) particle template image to be convolved with the filtered image and (*d*) convolution peak, the red cross indicating the detected particle centroid.

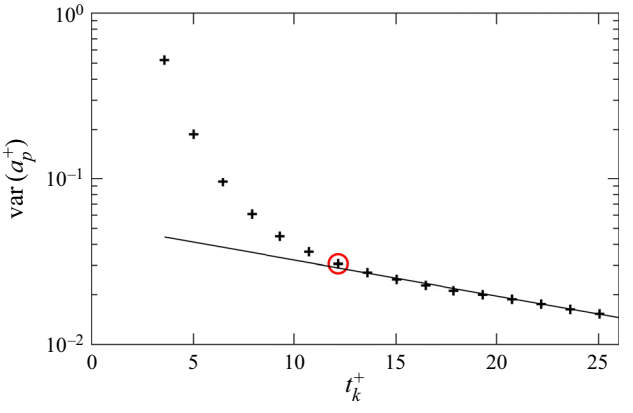

FIGURE 6. Streamwise acceleration variance as a function of smoothing kernel width. The solid line indicates the fit of the acceleration variance over its exponential range, and the optimal kernel width is denoted by the open circle.

in the 4×4 vector neighbourhood surrounding each particle (a 2×2 neighbourhood is used for $y^+ < 25$ to account for the greater shear). As the particles have finite size, this definition does not accurately represent an undisturbed fluid velocity at the particle location (as used in the correct definition of the drag force, Horwitz & Mani 2016), but it will serve the purpose of investigating the fluid flow events experienced by the particles.

To obtain particle velocities and accelerations, the particle trajectories are convolved with the first and second derivative of a Gaussian kernel, respectively. This method, introduced for fluid tracers (Voth *et al.* 2002; Mordant, Crawford & Bodenschatz 2004), has been used in several studies of inertial particles in turbulence (Gerashchenko *et al.* 2008; Nemes *et al.* 2017; Ebrahimian *et al.* 2019). The optimal width of the kernel t_k is determined from the variance of the particle acceleration magnitude in the data set: the latter is calculated for a range of kernel widths, and the smallest value for which the variance start decaying exponentially is adopted (figure 6). This corresponds to a duration of 17 successive snapshots, or about $12\tau^+$, where $\tau^+ = \nu/u_\tau$ is the time scale based on wall units.

2.5. *Measurement uncertainty*

Uncertainty in the particle statistics is estimated by considering both random uncertainty (due to the finite sample size) and bias uncertainty (due to imperfect centroid locations).

The random uncertainty is estimated by computing 90 % confidence intervals on the statistics (Bendat & Piersol 2011). The bias uncertainty is estimated by performing detection, tracking and smoothing on a set of synthetic particle images and comparing the position, velocity and acceleration of the smoothed tracks to the known values. The associated uncertainty on the particle location, defined as the root-mean-square (r.m.s.) difference between the actual and calculated values, is found to be approximately 0.04 mm (1 pixel), and therefore random error is the dominant source of uncertainty for particle statistics. To evaluate random uncertainty, we assume a number of independent realizations equal to the number of recorded trajectories. When statistics are computed within wall-normal bins, we assume a number of independent realizations equal to the number of trajectories in each bin.

Uncertainty in the PIV is also dominated by random error. The number of independent samples in the PIV statistics is estimated as the number of temporally independent realizations (i.e. the number of boundary-layer turnover times in the recording) multiplied by the number of spatially independent samples in each realization (i.e. w/δ_{99}, where δ_{99} is the boundary-layer thickness).

For the fluid velocity evaluated at the particle location, the interpolation also contributes to the uncertainty. This uncertainty is estimated by applying an artificial particle mask to images where the actual velocity vectors are known, performing PIV analysis on the masked images, then interpolating the resulting fluid velocity at the location of the artificial particles. The actual fluid velocity is then compared with the artificially interpolated values. The resulting interpolation error on the fluid velocity, again defined as the r.m.s. difference between the actual and calculated values, is approximately 1 mm s^{-1}, significantly smaller than the random error. The particles closest to (and in contact with) the wall are detected at $y^+ \approx D_p^+/2 = 8$, requiring an extrapolation from the nearest PIV vectors at $y^+ = 12$. While this may lead to larger uncertainties, these are not believed to overshadow any of the reported trends.

3. Results and discussion

3.1. *Fluid and particle velocity*

Here and in the following, the streamwise and wall-normal coordinates are indicated by x and y, respectively, and u and v indicate the respective velocity components. These are Reynolds decomposed as $u = \langle u \rangle + u'$ and $v = \langle v \rangle + v'$, where angle brackets denote the time average and the prime denotes the fluctuating part. Subscripts f and p denote quantities referring to fluid and particles, respectively, and the subscript $f|p$ denotes fluid quantities interpolated at the particle location. In figures 7 and 8, the particle-laden and unladen fluid velocity statistics are compared to turbulent boundary-layer measurements by De Graaff & Eaton (2000) at a similar Reynolds number ($Re_\theta = 1430$). The particle-laden and unladen fluid velocity profiles overlap within experimental uncertainty, indicating that significant two-way momentum coupling between the particles and fluid is not present. From the mean velocity profile, the friction velocity is determined by iterative fitting, with the von Kármán constant $\kappa = 0.41$ and the additive constant $B = 5.5$. The Reynolds stress profiles show some discrepancies in the magnitudes of the peak stresses due to the non-canonical features of the channel design (unconventional forcing, limited channel width) and limited spatial resolution. Physical parameters of the water channel and the boundary-layer properties are reported in table 3.

Profiles of particle velocity are obtained by defining wall-normal layers (bins) and taking the mean of particle velocities within each. Particles are more numerous near the wall and sparser in the outer region (approximately following a power law, see § 3.6), thus the

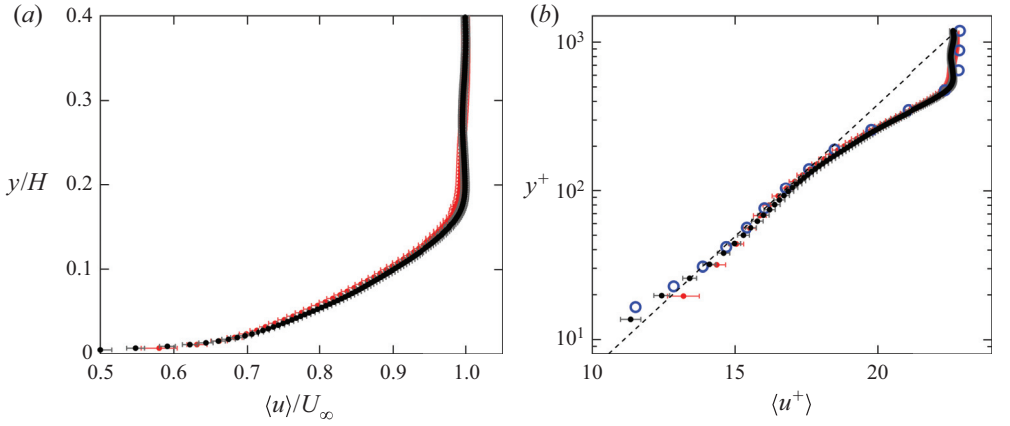

FIGURE 7. Mean streamwise velocity profile of the particle-laden (black dots) and unladen (red dots) fluid, in (*a*) outer units and (*b*) wall units. The dashed line in (*b*) indicates the logarithmic-law fit. The profile is compared with De Graaff & Eaton (2000) in (*b*), shown in blue open circles.

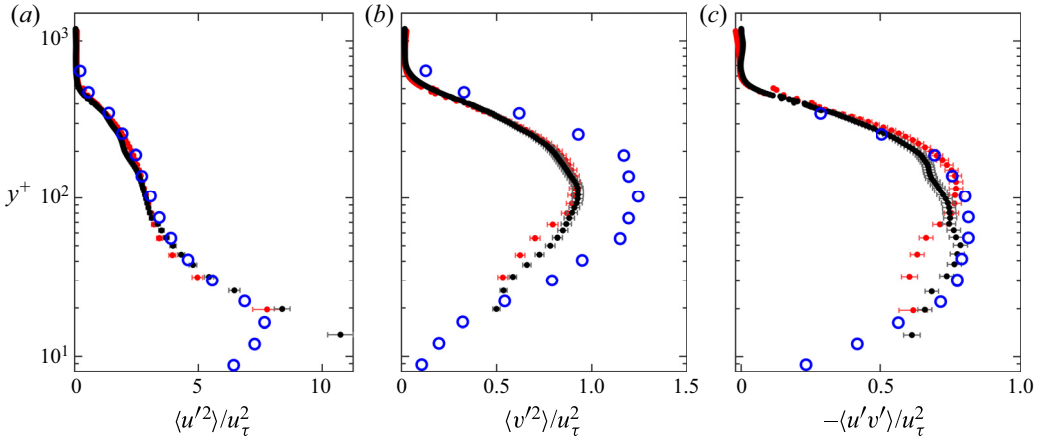

FIGURE 8. Profiles of particle-laden (black dots) and unladen (red dots) streamwise turbulent normal stress (*a*), wall-normal normal stress (*b*) and shear stress (*c*) of the fluid in wall units. The profiles are compared with De Graaff & Eaton (2000) shown in blue open circles.

U_∞ (m s^{-1})	H (mm)	W (mm)	δ_{99} (mm)	u_τ (mm s^{-1})	Re	Re_τ	Re_θ
0.42	150	150	29	18.5	66 000	570	1270

TABLE 3. Physical parameters of the water channel and boundary-layer properties. U_∞ is the free-stream velocity, H is the water depth, W is the channel width, δ_{99} is the boundary-layer thickness and u_τ is the shear velocity. The boundary thickness is defined such that $u(\delta_{99}) = 0.99U_\infty$; $Re = U_\infty H/\nu$, $Re_\tau = u_\tau \delta_{99}/\nu$ and $Re_\theta = U_\infty \theta/\nu$ are the free-stream, friction and momentum thickness Reynolds numbers, respectively. Standard water properties at 22 °C are used in the calculations.

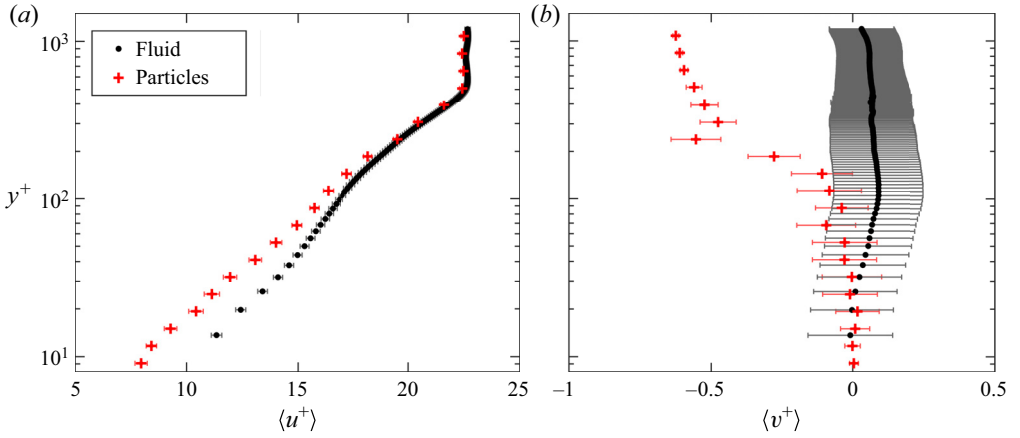

FIGURE 9. Wall-normal profiles of streamwise (*a*) and wall-normal (*b*) mean particle velocity (red crosses) compared with the mean fluid velocity (black dots).

bins are logarithmically spaced to equalize the numbers of particles in each, as well as to capture the high shear in the near-wall region. The mean streamwise and wall-normal particle velocity profiles are shown in figure 9. In the free stream, the particle streamwise velocity is very similar to the fluid's (figure 9*a*), as expected since there the particles are in equilibrium with a steady flow having negligible fluctuations. Closer to the wall ($y^+ \lesssim 200$) the particles generally lag the fluid, due to their inertia in responding to turbulence. Past experiments found that mean velocity of inertial particles exceeded that of the fluid in the viscous sublayer; see Kaftori *et al.* (1995*a*), Righetti & Romano (2004) and Ebrahimian *et al.* (2019). The present PIV resolution does not allow reliable measurements at such small heights, but the canonical shape of the boundary-layer profile suggests that the lag is vanishing approaching the wall. We remark that those previous studies considered smaller particles (in wall units) whose centroid could reach closer to the wall.

The vertical velocity profile (figure 9*b*) shows that in the free stream the particles settle through the fluid at a speed close to the still-fluid terminal velocity. This is again consistent with the fact that particles at those heights fall through a quasi-laminar flow. For $y^+ \lesssim 200$ (the same range for which particles lag the fluid streamwise velocity), the vertical velocity decays in magnitude, but remains negative. We note that a downward mean particle velocity is expected under equilibrium conditions, i.e. when the wall-normal turbulent flux balances the gravitational settling (Rouse 1937; Prandtl 1952). Using the concentration measurements (see § 3.6), we estimate the total vertical flux to be several orders of magnitude smaller than the streamwise flux, confirming approximate equilibrium conditions. The Rouse–Prandtl theory, however, assumes a constant settling velocity (generally taken to be equal to the still-fluid terminal velocity) throughout the boundary layer, while here it shrinks to vanishingly small values approaching the wall. We investigate the roots of this effect, as well as the streamwise velocity lag, in the following.

3.2. *Slip velocity*

The reduced streamwise velocity of the particles has been often attributed to the preferential sampling of slow fluid regions (Kaftori *et al.* 1995*a*; Kiger & Pan 2002). We investigate this issue first by separating the mean slip velocity ($\langle u_p \rangle - \langle u_f \rangle$) in two separate contributions: the 'particle-conditioned' slip velocity, i.e. the mean slip velocity

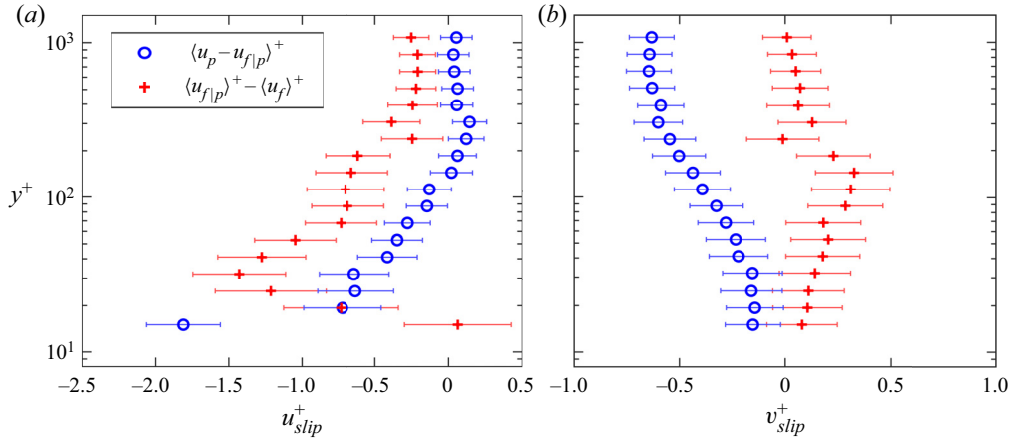

FIGURE 10. Wall-normal profiles of mean streamwise (*a*) and wall-normal (*b*) particle slip velocity, separated into the particle-conditioned mean slip (blue circles) and the apparent mean slip (red crosses).

at the particle location, $\langle u_p - u_{f|p}\rangle$, and the 'apparent' slip velocity due to the oversampling of fluid regions faster or slower than the average, $\langle u_{f|p}\rangle - \langle u_f\rangle$ (Kiger & Pan 2002)

$$\langle u_p\rangle - \langle u_f\rangle = \langle u_p - u_{f|p}\rangle + \langle u_{f|p}\rangle - \langle u_f\rangle. \tag{3.1}$$

Figure 10(*a*) displays both contributions. (We only report the slip velocity down to the location of the PIV vector closest to the wall, to avoid extrapolation.) It indicates that, for $y^+ > 20$, the particles do oversample fluid regions with negative streamwise fluctuations ($\langle u_{f|p}\rangle - \langle u_f\rangle < 0$). Closer to the wall, however, the particle-conditioned slip plays a dominant role in determining the particle lag from the fluid: the term $\langle u_p - u_{f|p}\rangle$ becomes larger in magnitude than $\langle u_{f|p}\rangle - \langle u_f\rangle$. This is consistent with the recent findings of Berk & Coletti (2020) who considered solid particles in air at much larger Re_τ and a broad range of St^+.

A similar decomposition can be carried out for the vertical velocity component, noting that $\langle v_f\rangle = 0$:

$$\langle v_p\rangle = \langle v_p - v_{f|p}\rangle + \langle v_{f|p}\rangle, \tag{3.2}$$

which highlights the separate contributions of the particle-conditioned slip and the vertical fluid velocity at the particle location. Figure 10(*b*) shows that the first term on the right-hand side dominates in the free stream and decreases approaching the wall. The second term, representing the preferential sampling of upward/downward fluid fluctuations, is negligible in the free stream and it becomes comparable to the first term as the wall is approached. In particular, particles near the wall oversample upward fluid motions ($\langle v_{f|p}\rangle > 0$). This is consistent with their tendency of favouring negative streamwise fluctuations, which are correlated with upward fluctuations in a turbulent shear flow. This point will be further discussed in § 3.4. In general, throughout the boundary layer, the effect of the turbulence on the particle settling is opposite to what one would expect from homogeneous turbulence studies, where the predominant effect is the enhancement of settling speed by preferential sweeping (Wang & Maxey 1993; Petersen *et al.* 2019).

The mean particle-conditioned slip velocity can be used to define profiles of particle Reynolds numbers, $Re_{p,u_{slip}} = \langle u_p - u_{f|p}\rangle D_p/\nu$ and $Re_{p,v_{slip}} = \langle v_p - v_{f|p}\rangle D_p/\nu$,

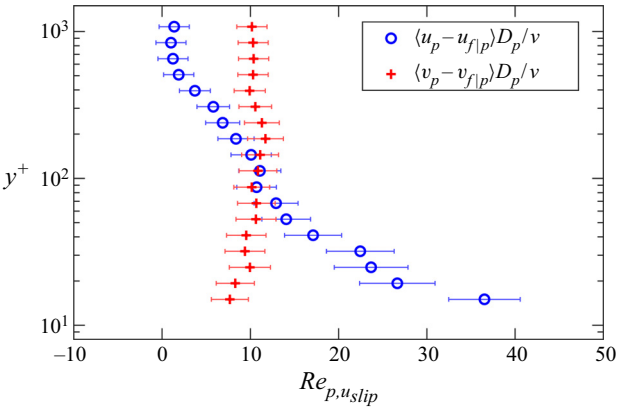

FIGURE 11. Profiles of mean instantaneous particle Reynolds number based on the particle-conditioned streamwise (blue circles) and wall-normal (red crosses) slip velocity.

shown in figure 11. Given the observed ranges, the particle wakes are likely to extend for less than one diameter (Rimon & Cheng 1969). At the present volume fraction, particles are hardly ever found so close to each other, indicating that the momentum coupling between particles can be assumed to be negligible. However, the Reynolds numbers are well into the nonlinear drag regime, especially in the near-wall region. While drag corrections are available (Clift *et al.* 2005), those are developed for steady/quiescent flows. In a turbulent flow laden with particles at finite Re_p, the nonlinearities undermine the use of superposition (assumed in the derivation of the particle equation of motion, Maxey & Riley 1983), making the particle–fluid dynamics challenging to capture with point-particle simulations (Wang *et al.* 2019).

The instantaneous slip experienced by the particles with respect to the surrounding fluid is related to their ability to retain memory of the flow events experienced at previous times. Thus, one might infer that the gravitational drift plays a major role in determining the streamwise slip velocity, as the settling particles cross flow trajectories and attain large relative velocities with respect to the fluid. This view is certainly valid in homogeneous turbulence (e.g. Csanady 1963; Elghobashi & Truesdell 1992). In a turbulent boundary layer, however, the tendency of the particles to sample slow flow regions, combined with the mean wall-normal velocity gradient, leads to a different outcome. Let us consider separately the mean streamwise velocity profile for ascending and descending particles; that is, particles with positive and negative instantaneous vertical velocity, respectively. Figure 12(*a*) shows that ascending particles, on average, move slower than the fluid and account for most of the mean slip velocity reported above; while descending particles roughly match the mean fluid velocity in the outer layer. This trend, in agreement with Kiger & Pan (2002) and van Hout (2011), is explained by the fact that ascending particles come from slower-moving regions of the flow nearer to the wall, and therefore have lower streamwise velocities. Therefore, unlike in homogeneous flows, it is the ascending particles suspended by the turbulence that determine the large slip velocity, rather than the descending ones that settle due to gravity. Remarkably, the vertical velocity of the ascending particles is comparable in magnitude to that of the descending ones, both being the order of the friction velocity. As the descending particles near the wall are more numerous, their contributions dominate the statistics and the mean vertical velocity of the dispersed phase is negative.

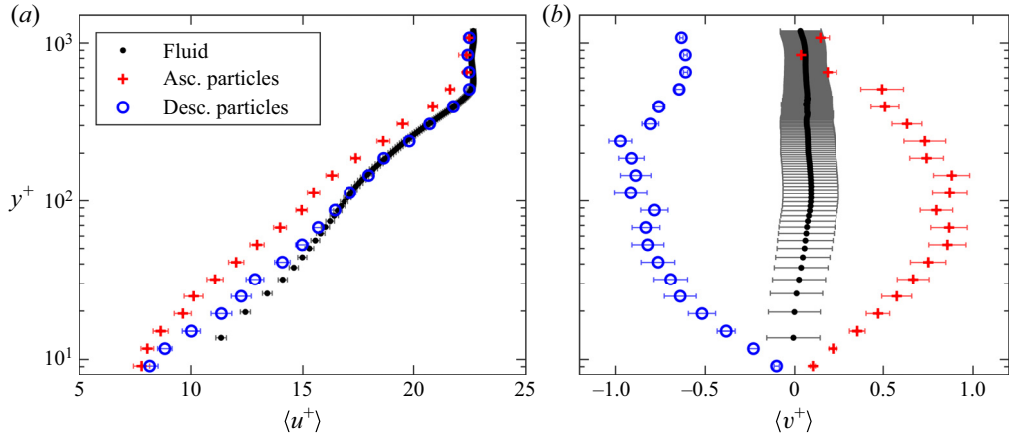

FIGURE 12. Profiles of mean streamwise (*a*) and wall-normal (*b*) particle velocity conditioned on ascending (red crosses) and descending (blue circles) particles compared to the fluid velocity (black dots).

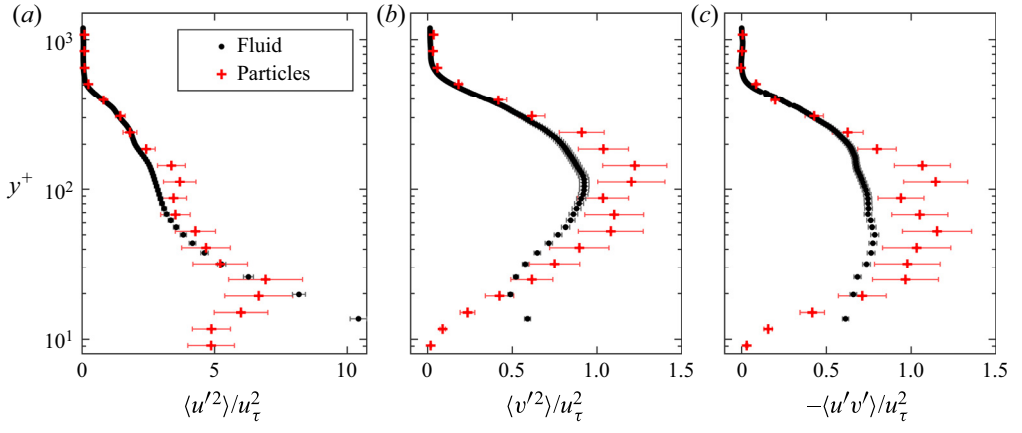

FIGURE 13. Wall-normal profiles of the Reynolds stresses of the particles (red crosses) and fluid (black dots) normalized by the squared shear velocity.

3.3. *Reynolds stresses*

Profiles of particle and fluid Reynolds stresses are compared in figure 13. The streamwise normal stress of the particles are comparable to that of the fluid, while the particle wall-normal normal stress and shear stress exceed that of the fluid in the range $20 \lesssim y^+ \lesssim 200$. Qualitatively similar results were reported for particles in water (Kaftori, Hetsroni & Banerjee 1995*b*; van Hout 2011) and in air (e.g. Tanière *et al.* 1997; Fong, Amili & Coletti 2019). The relatively large particle velocity fluctuations are interpreted as a consequence of the spread in momentum of particles with different pathways, retaining memory of their interactions with disparate flow structures. This in turn results in particles often being surrounded by fluid with velocity different from their own, contributing to the instantaneous slip reported above.

To explore the particle–turbulence interaction, we again condition the fluid statistics on the location of ascending and descending particles. The Reynolds shear stresses are

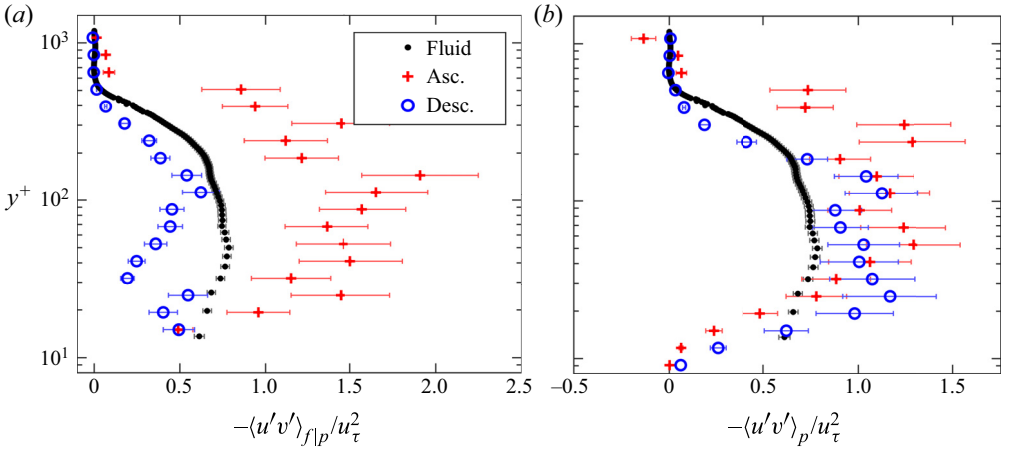

FIGURE 14. Wall-normal profiles of the Reynolds shear stress of (*a*) the fluid velocity at particle locations and (*b*) the particle velocity, conditioned on ascending and descending particles (red crosses and blue circles, respectively). The profiles are compared to the overall fluid shear stress profile (black dots).

of special interest: they feature in the turbulence production and represent the statistical signature of the instantaneous sweep and ejection events that are believed to play a crucial role in the particle transport (Marchioli & Soldati 2002). Figure 14(*a*) displays the fluid Reynolds shear stress evaluated at the locations of ascending and descending particles, while figure 14(*b*) shows the 'particle Reynolds shear stress' associated with ascending and descending particles. The ascending particles appear to sample regions with much larger fluid shear stress magnitudes compared to the descending particles, while the shear stress magnitudes of ascending and descending particles themselves are nearly the same. That suggests that the motion of the former is strongly driven by turbulent ejection events, while the latter have a weaker relation to sweep events.

3.4. *Quadrant analysis*

Previous work (e.g. Niño & Garcia 1996; Kiger & Pan 2002; Marchioli & Soldati 2002; van Hout 2011) found evidence that inertial particles are strongly affected by sweep and ejection events in the turbulent boundary layer. Sweeps are identified as simultaneous $u_f' > 0$ and $v_f' < 0$ events (fourth quadrant of the u_f'–v_f' plane, or Q4) and ejections as simultaneous $u_f' < 0$ and $v_f' > 0$ (second quadrant, or Q2). They are often associated with coherent structures in wall turbulence, such as streamwise rollers and hairpin vortices (Robinson 1991). We first plot in figure 15 the joint PDF of streamwise and wall-normal fluid velocity fluctuations: for the near-wall region ($y^+ < 100$, figure 15*a*) and farther away from the wall ($y^+ > 100$, figure 15*b*). As expected, sweeps and ejections are dominant near the wall, whereas away from the wall the fluctuations are weaker and there are no dominant quadrants. We then consider the quadrant events at the location of ascending and descending particles, in the near-wall and outer regions. Near the wall, ascending particles are found to strongly oversample ejection events (figure 15*c*), supporting the view that ejections are a major mechanism driving particle resuspension. Even in the outer region, although the ejections themselves are weaker, ascending particles still occupy the second quadrant almost exclusively (figure 15*d*). In contrast, descending particles are found to oversample sweep events near the wall, but the preference is weaker (figure 15*e*), and in the

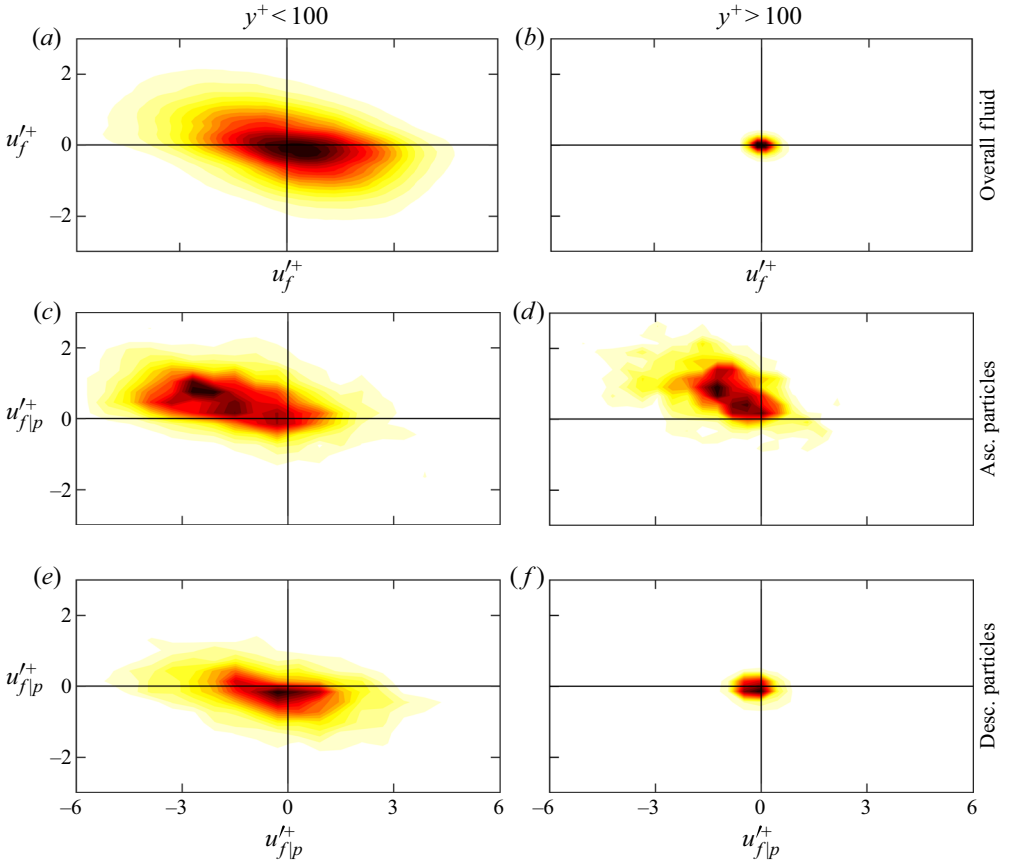

FIGURE 15. Joint PDFs of streamwise and wall-normal fluctuating fluid velocities for $y^+ < 100$ (*a*) and $y^+ > 100$ (*b*). Joint PDFs of streamwise and wall-normal fluctuating fluid velocities at particle locations for $y^+ < 100$ (*c*,*e*) and $y^+ > 100$ (*d*,*f*) conditioned on whether the particle is ascending (*c*,*d*) or descending (*e*,*f*).

outer region, descending particles do not preferentially sample any quadrant (figure 15*f*). This indicates that sweeps weakly influence the descent of particles towards the wall, while ejections are a key factor in lifting the particles away from the wall.

The prevalence of fluid ejection over sweeps in influencing particle transport was reported by previous studies focused on heavy particles suspended in horizontal wall-bounded flows over a wide range of physical parameters (Kiger & Pan 2002; van Hout 2011; Li *et al.* 2012; Zhu *et al.* 2019; Berk & Coletti 2020). This is in contrast with configurations in which gravity does not participate to the wall-normal transport: in no-gravity simulations (e.g. Marchioli & Soldati 2002) and in vertical channel flow experiments (e.g. Fong *et al.* 2019) sweep events crucially contribute to the turbophoretic drift that produces a multi-fold increase in near-wall concentration. In horizontal particle-laden flows, by contrast, the near-wall concentration has been found to be smaller than what predicted by the Rouse–Prandtl equilibrium theory (Kiger & Pan 2002; Zhu *et al.* 2019; Berk & Coletti 2020). In § 3.6 we will show this to be the case also in the present configuration. Because the Rouse–Prandtl theory does not account for turbophoresis, we deduce the latter is not playing a significant role in the particle transport

for the present conditions, despite St^+ being in the turbophoretic regime according to point-particle simulations without gravity (see, e.g. Bernardini 2014). This could be partly due to the relatively large size of our particles, which influences the ability of inner-layer streamwise vortices to accumulate them at the wall. However, considering the findings of previous studies with much smaller particles (e.g., Berk & Coletti 2020), the more likely reason is that gravitational drift disrupts the particle interaction with coherent turbulent motions.

3.5. *Particle diffusion*

The question of dispersion is central in particle-laden flows. A large body of experimental and numerical work in homogeneous turbulence has established that heavy particles disperse differently from tracers due to two distinct and competing effects. Particle inertia increases the integral time scale of their Lagrangian velocity autocorrelation, and hence their diffusivity, due to the finite response time (Squires & Eaton 1991; Wang & Stock 1993; Jung, Yeo & Lee 2008). Meanwhile, particle drift due to gravity or other body forces causes them to cross fluid trajectories with consequent decorrelation of motion and reduction of diffusivity compared to tracers (Csanady 1963; Squires & Eaton 1991; Elghobashi & Truesdell 1992; Wang & Stock 1993). In wall-bounded flows, Lagrangian stochastic models have been proposed in order to predict dispersion of inertial particles (Tanière & Arcen 2016; Marchioli 2017) but have been mostly tested against point-particle numerical simulations, usually without gravity.

To address the issue of dispersion, we first consider the temporal coherence of particle motion by computing Lagrangian autocorrelations of the particle velocity (in these definitions we only refer to u_p for brevity, but all definitions apply to v_p as well), given by

$$\rho_{u_p}(\Delta t, y_0) = \frac{\langle u_p'(t_0, y_0) u_p'(t_0 + \Delta t, y_0)\rangle}{\langle u_p'(t_0, y_0) u_p'(t_0, y_0)\rangle}. \tag{3.3}$$

The subscript '0' denotes the origin of a trajectory, so that t_0 and y_0 are the initial time and wall-normal location of each trajectory, respectively. Here, the fluctuating velocities, u_p', are determined by subtracting the Lagrangian mean velocity from each trajectory, $\langle u_p(\Delta t, y_0)\rangle_L$, as follows:

$$u_p'(t_0 + \Delta t, y_0) = u_p(t_0 + \Delta t, y_0) - \langle u_p(\Delta t, y_0)\rangle_L. \tag{3.4}$$

The Lagrangian autocorrelation is computed within five logarithmically spaced wall-normal bins, such that each contains a comparable number of samples. The autocorrelations of streamwise and wall-normal particle velocities are plotted in figures 16(*a*) and 16(*b*), respectively. They both drop off more steeply near the wall, and the streamwise particle velocity remains correlated over a longer length of time than the wall-normal velocity. These trends are consistent with results for fluid tracers in channel flow simulations (Choi, Yeo & Lee 2004). They are attributed to the smaller flow scales affecting the particle motion near the wall, and the streamwise-elongated structures that characterize the boundary layer, contributing to the turbulence anisotropy.

The integral time scale of the particle motions in streamwise and wall-normal directions can be defined as $\tau_{L,x} = \int_0^\infty \rho_{u_p}(\Delta t)\,\mathrm{d}t$ and $\tau_{L,y} = \int_0^\infty \rho_{v_p}(\Delta t)\,\mathrm{d}t$, respectively. Since in practice the integral can only extend to finite values, and recognizing that ρ_{u_p} and ρ_{v_p} approximately follow an exponential decay, we fit an exponential function to the autocorrelations and consider the time lag that results in an e-fold drop of the

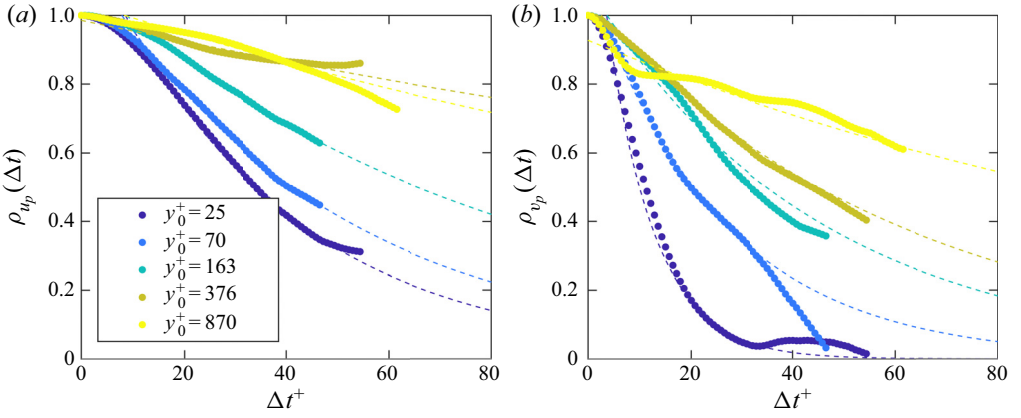

FIGURE 16. Lagrangian autocorrelations of streamwise (*a*) and wall-normal (*b*) particle velocity for five wall-normal bins (dots) shown with their respective exponential fits (dashed lines). The wall-normal locations listed in the legend correspond to the centre of each bin.

exponential fit. Applying the theory of Taylor (1921) on the Lagrangian statistics of particle displacements, we evaluate the long-time particle diffusivities in both directions, $\varepsilon_{p,x} = \tau_{L,x}\langle u_p'^2\rangle$ and $\varepsilon_{p,y} = \tau_{L,y}\langle v_p'^2\rangle$. In figure 17 this is shown for the five wall-normal bins and for both velocity components, computed using the variance of the particle velocity within the respective bins. For comparison, we also plot the classic estimate for the fluid momentum diffusivity in the log-law region, $\varepsilon_f = \kappa y u_\tau$ (Prandtl 1952), and that for the defect layer ($y > 0.2\delta_{99}$), estimated as $\varepsilon_f = 0.09\delta_{99}u_\tau$ (Pope 2000). In the log-law region, the turbulence causes the particles to disperse much faster in the streamwise direction, greatly exceeding the momentum diffusivity. This indicates that the effect of particle inertia (which increases particle dispersion) is dominating over the effect of gravitational drift (which reduces it), at least in what pertains streamwise dispersion. This agrees with theoretical arguments of Reeks (1977) which predicted particles to disperse faster than tracers when the settling velocity $V_s < \langle u_f'^2\rangle^{1/2}$, as it is the case here. Laboratory observations had confirmed this in homogeneous turbulence (Wells & Stock 1983; Sabban & van Hout 2011), and to our knowledge the present results are the first experimental observation of this effect in wall turbulence. On the other hand, $\varepsilon_{p,y}$ is equal to or smaller than the momentum diffusivity across the boundary layer, indicating that, in the vertical direction, the effect of gravity in decorrelating the particle motion slightly dominates.

3.6. *Particle concentration and flux*

Mean particle relative concentration as a function of wall-normal distance is plotted in figure 18. This is obtained by counting particles within logarithmically spaced wall-normal bins and normalizing by the mean concentration in the lowest bin, C_0. The observed power-law behaviour prompts a comparison with the concentration profile predicted by the theory of Rouse (1937) and Prandtl (1952). This follows from the balance between gravitational settling and wall-normal turbulent flux

$$\langle C\rangle V_s - \varepsilon\frac{\partial\langle C\rangle}{\partial y} = \Phi, \tag{3.5}$$

where V_s is the particle settling velocity and Φ is the net wall-normal flux of particles. Assuming equilibrium conditions ($\Phi = 0$), the particles falling at $V_s = V_t$ and having the

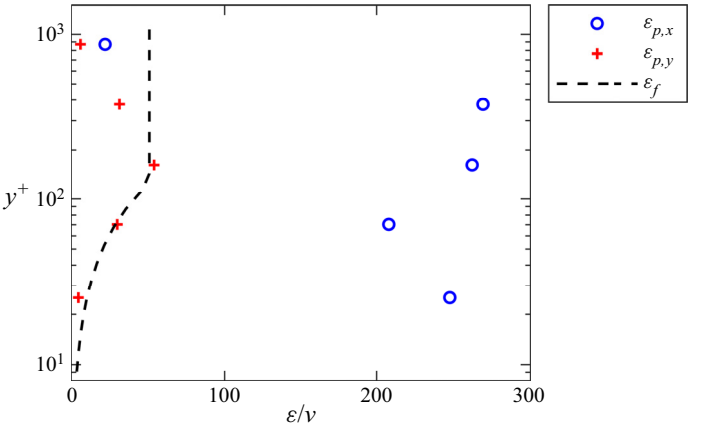

FIGURE 17. Wall-normal profiles of streamwise and wall-normal diffusivity (blue circles and red crosses, respectively) compared to the theoretical profile of fluid momentum diffusivity (black dashed line).

same diffusivity as the momentum in the turbulent boundary layer ($\varepsilon = \kappa y u_\tau$), leads to the well-known concentration profile (Prandtl 1952)

$$\frac{\langle C\rangle}{\langle C\rangle_{ref}} = \left(\frac{y}{y_{ref}}\right)^{-Ro}, \tag{3.6}$$

where the subscript denotes an arbitrary reference height and the corresponding concentration. Here, $Ro = -V_t/(\kappa u_\tau)$ is the Rouse number, which quantifies the relative strength of gravitational settling and turbulent resuspension of the particles. Equation (3.6) is also plotted in figure 18 for comparison, which shows a much steeper drop in concentration with height than the measurements. A departure from Rouse–Prandtl theory is expected, notably because the latter does not account for particle inertia. In particular, Berk & Coletti (2020) recently carried out a wind tunnel study of particle transport in turbulent boundary layers, and also reported a reduced slope of the concentration profile compared to the Rouse–Prandtl theory for a wide range of Stokes numbers. They hypothesized this to be due to a near-wall settling rate below the terminal velocity but could not accurately measure the particle vertical velocity. The present measurements corroborate their hypothesis (see figure 9*b*).

The particle streamwise mass flux Q_x is often of interest, especially in geophysical flows. Assuming advection dominates on the turbulent transport, the mean flux can be approximated from the mean concentration and mean velocity profiles, i.e. $\langle Q_x\rangle \approx \langle C\rangle\langle u_p\rangle$. Here, we compute the flux directly by counting particles crossing wall-normal planes, and verify that it does not vary with streamwise location within the imaging window, and that it is indistinguishable from the mean advective flux $\langle C\rangle\langle u_p\rangle$. The profile in figure 19, albeit with experimental scatter, suggests a power-law behaviour. In sediment transport and aeolian transport studies, the flux is often observed to decay exponentially with wall-normal height, thus identifying a characteristic length scale (e.g. Bagnold 1941; Nishimura & Hunt 2000; Guala *et al.* 2008; Kok *et al.* 2012). However, those processes are inherently different from the present one: they are characterized by beds of particles mobilized by the impact of other particles, with their transport largely concentrated in a 'saltation layer'. The present case instead is governed by suspension, and as such it does not possess a specific length scale beyond those associated with the fluid turbulence.

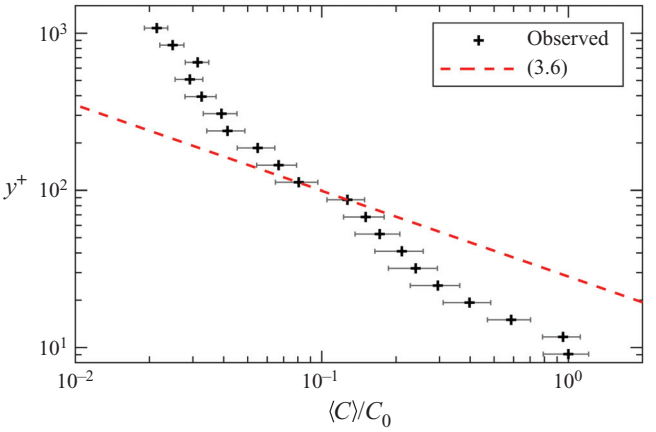

FIGURE 18. Wall-normal profile of mean particle concentration normalized by the concentration at the lowest wall-normal bin (black crosses). The power-law profile predicted by Rouse–Prandtl theory (red dashed line) is calculated from (3.6), where the arbitrary reference height is taken at $y_r^+ = 90$.

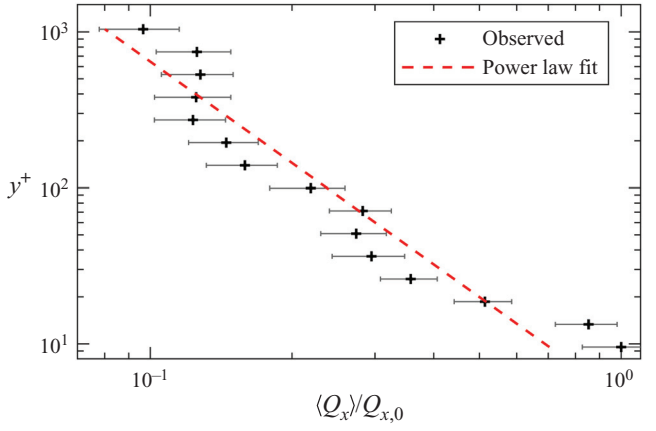

FIGURE 19. Wall-normal profile of particle streamwise mass flux normalized by the mass flux at the lowest wall-normal bin (black crosses), compared with a power-law fit (red dashed line).

3.7. *Particle acceleration*

The statistics of the particle acceleration provide insight not only on the kinematics but also on the forces at play. In figure 20(*a*) we present the profiles of mean and r.m.s. acceleration for both in-plane components. The mean acceleration profiles are in close agreement with the recent experiments of Ebrahimian *et al.* (2019), who considered particles with $St^+ = 3.9$ and $D_p^+ = 6.8$ in a channel flow at $Re_\tau = 410$. The mean acceleration is negligible in the free stream, as expected in a fully developed flow. The streamwise acceleration increases to a positive maximum at $y^+ \sim 50$, and then rapidly decays to become negative near the wall. When expressed in wall units, the negative mean streamwise acceleration we observe near the wall is significantly smaller in magnitude compared with the experiments of Gerashchenko *et al.* (2008). These authors considered microscopic water droplets, and therefore the discrepancy is likely rooted in the larger size

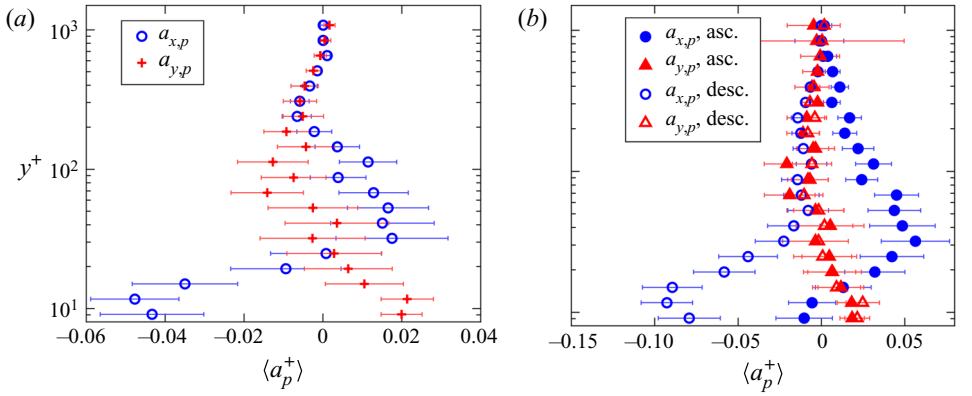

FIGURE 20. (*a*) Profiles of mean streamwise and wall-normal particle acceleration. (*b*) Profiles of mean streamwise and wall-normal particle acceleration conditioned on whether particles are ascending (filled symbols) or descending (open symbols).

of our particles compared to the viscous length scale, and the consequent effect of forces other than drag and gravity (Maxey & Riley 1983). The difference could also be related to particle interactions with the wall (addressed in § 3.8), which were likely inconsequential for the statistics of Gerashchenko *et al.* (2008).

The mean wall-normal acceleration shows a qualitatively opposite trend compared to the streamwise component. At first, this would appear consistent with sweep and ejection being at the root of the acceleration profiles: upward vertical fluid fluctuations lifting the particles away from the wall also tend to decelerate them in streamwise direction, and *vice versa* for downward fluctuations. This view, however, does not consider the fact that the mean velocity of the particles is downward: thus, negative wall-normal accelerations are mostly associated with a decrease in magnitude of the negative velocity, i.e. hindering of the settling. We shall come back to this point shortly, when considering the fluid events associated with these particle statistics.

In Gerashchenko *et al.* (2008) and Lavezzo *et al.* (2010) it was argued that the gravitational settling of particles through the shear flow plays a crucial role in determining the streamwise acceleration. To explore this issue, we condition again the statistics on ascending and descending particles (figure 20*b*). It becomes apparent that the regions of positive and negative streamwise acceleration can be attributed to the ascending and descending particles, respectively. This is in line with arguments presented by Gerashchenko *et al.* (2008) and Ebrahimian *et al.* (2019): particles that fall vertically find themselves surrounded by slower fluid, which decelerates them; and *vice versa* for particles moving vertically upward. The mean vertical acceleration is instead unaffected by conditioning on ascending/descending particles.

We present profiles of r.m.s. particle acceleration in figure 21. The streamwise component is quantitatively close to what is reported by Gerashchenko *et al.* (2008), Zamansky *et al.* (2011) and Ebrahimian *et al.* (2019). The wall-normal component instead reaches a peak 30 %–60 % larger than in those studies, being comparable to the streamwise component. We believe this to be mainly caused by gravitational effects. Already Gerashchenko *et al.* (2008) found that the particle r.m.s. acceleration of inertial particles was larger than that of tracer particles, in contrast with known trends in homogeneous turbulence (Bec *et al.* 2006; Ayyalasomayajula *et al.* 2006). Our particles are more inertial than those considered by Gerashchenko *et al.* (2008) (who had maximum

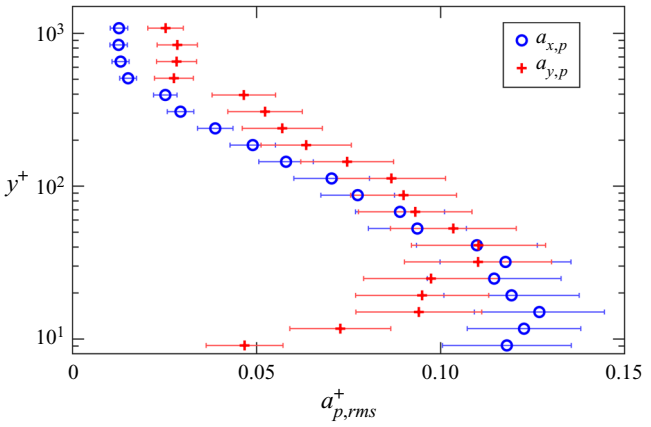

FIGURE 21. Wall-normal profiles of streamwise (blue circles) and wall-normal (red crosses) particle r.m.s. acceleration.

$St^+ = 5.3$) and have larger settling velocity ($V_t/u_\tau = 0.75$, versus $V_t/u_\tau = 0.38$ in that study). In laboratory experiments it is not possible to conclusively disentangle inertia from gravity to determine what drives the higher vertical r.m.s. acceleration, but we can find hints in previous numerical studies where gravity could be suppressed. Lavezzo *et al.* (2010) demonstrated that gravity was the cause of increased r.m.s. acceleration in streamwise direction. This appears to be the case also for the wall-normal component, enhanced because the falling particles encounter rapidly changing flow structures. In further support of this view, the zero-gravity simulations of Zamansky *et al.* (2011) found a decrease of both components of r.m.s. acceleration with increasing St^+, while the recent simulations of Lee & Lee (2019) that included gravity showed the opposite trend, in agreement with Gerashchenko *et al.* (2008). Taken together, the above indicates that it is gravitational drift that causes heavy particles to have large r.m.s. accelerations, in both streamwise and wall-normal directions.

The acceleration of fluid tracers and inertial particles in turbulence are known to be intermittent, with super-Gaussian probabilities of high-acceleration events that strongly depend on the particle inertia. When gravity is absent or has negligible influence, it is established that increasing Stokes number leads to reduced intermittency (Bec *et al.* 2006; Gerashchenko *et al.* 2008; Zamansky *et al.* 2011). We present the PDF of streamwise and wall-normal accelerations in figure 22. We plot separately the distributions for particles below and above $y^+ = 100$, which helps in better understanding the observed behaviour. The stretched exponential tails indicate significant intermittency, with relatively large probability of extreme events. This is, however, much stronger for the particles far from the wall than for those close to it: the flatness of the distributions for $y^+ < 100$ and $y^+ > 100$ is 5.5 and 20.5 for the streamwise component, and 6.4 and 10.4 for the wall-normal component, respectively. This is because the particles closer to the wall interact with turbulent eddies of smaller time scales, and therefore have an effectively larger Stokes number (see figure 4*a*), which in turn causes them to 'filter out' intense fluid flow events (Bec *et al.* 2006). The crossing-trajectory effect, on the other hand, is weaker for the near-wall particles, which have small mean vertical velocity (figure 9*b*). Combined with the results for the r.m.s. accelerations, these results underscore the competing influence of gravity and inertia: the first enhances the variance and intermittency of the particle

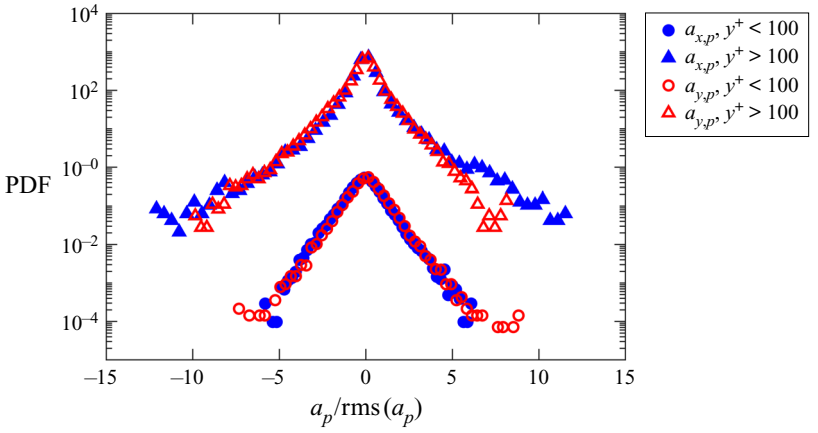

FIGURE 22. PDFs of streamwise (blue filled symbols) and wall-normal (red open symbols) particle acceleration conditioned on $y^+ < 100$ (circles) and $y^+ > 100$ (triangles). The PDFs for $y^+ > 100$ are shifted upward by a factor of 10^3 for clarity.

accelerations, while the second damps them, the net result depending on the relative importance of both effects.

The particle trajectories are influenced not only by the instantaneous values of their accelerations, but also by their temporal coherence. This is explored by calculating the Lagrangian autocorrelation of streamwise particle accelerations, defined analogously to the velocity autocorrelations and presented in figure 23 for various wall distances. The wall-normal acceleration (not shown) follows similar trends, but less clearly so due to experimental uncertainty on measuring quantities of smaller magnitude. Close to the wall ($y^+ \lesssim 100$), the acceleration has significant temporal coherence, with the autocorrelation showing *e*-folding time of the order of the response time of the particles, before decaying monotonically to zero. This suggests that near-wall particles move in and out of streamwise-coherent turbulent structures and behave as if responding to step changes in the surrounding fluid velocity. We will show in § 3.8 that this picture is consistent with the behaviour of the particles that directly interact with the wall. At larger heights, the temporal coherence is greatly reduced and the oscillations around zero suggest a quick alternation of positive and negative accelerations. This is likely caused by settling with significant speed (close to the particle terminal velocity for $y^+ \gtrsim 100$, see figure 9*b*), which causes the particles to move in a less coherent fashion. This is in line with the above-mentioned drop in streamwise diffusivity with increasing distance from the wall (figure 17).

3.8. *Particle–wall interactions*

In order to analyse the direct interactions with the wall, we consider the trajectories of particles that come in contact with it. An example of one such trajectory is shown in figure 24. Actual physical contact cannot be ascertained by the present imaging, and a lubrication layer is possibly maintained during those events. Still, we will use the word ‘contact’ to indicate the instances with no measurable wall–particle separation. More precisely, considering the variance of the particle diameters and the uncertainty in locating both the particles and the wall, we record contact when particle centroids are within 1.3 mean particle radii from the wall, i.e. when their wall-normal height is $y^+ \leqslant 10.4$.

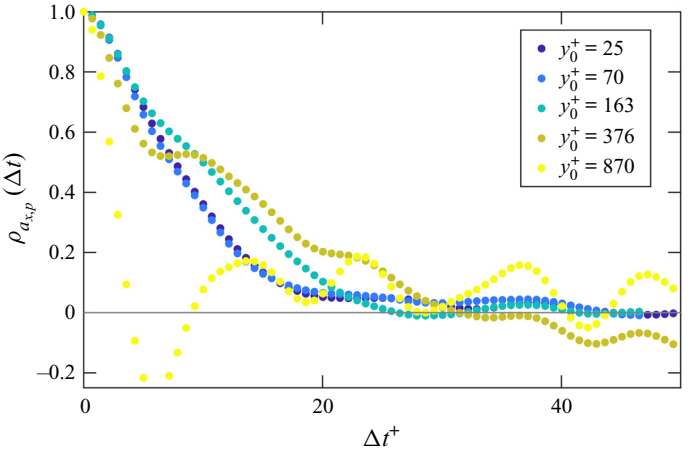

FIGURE 23. Lagrangian autocorrelation of streamwise particle acceleration for five wall-normal bins. The wall-normal locations listed in the legend correspond to the centre of each bin.

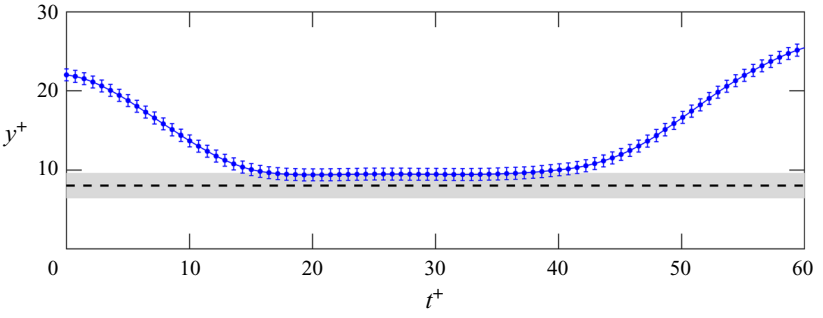

FIGURE 24. An example of an interaction between a particle and the wall. The blue curve shows the wall-normal distance of the particle centroid vs. time, with error bars representing the uncertainty in particle position. The dashed line represents a height of one particle radius above the wall, with the grey shaded region indicating the uncertainty in the particle radius and the wall location.

The results below are robust to small modifications of this threshold. We define 'touch-down' and 'lift-off' events when this threshold is crossed by particles approaching and leaving the wall, respectively. In figure 24, touch-down occurs at about $\tau^+ = 15$ and lift-off at about $\tau^+ = 40$; in between, the particle is considered to be in continued contact with the wall. Below we present results from averaging 241 trajectories leading to a touch-down and 151 trajectories following a lift-off.

First, particle–wall interactions are characterized in terms of duration of contact, t_{wall}. Figure 25 presents the PDF of t_{wall} in viscous units, which is well described by an exponential distribution. This is reminiscent of the distribution of 'waiting times' between touch-down and lift-off of the particles mobilized by the flow over a sediment bed (Einstein 1950; Ancey *et al.* 2006; Fan *et al.* 2016). In the case of bedload transport, an exponential distribution follows from assuming that touch-down and lift-off are time- and space-invariant Markovian processes (Ancey *et al.* 2006), i.e. independent events that are influenced only by the present and local state. Accordingly, waiting times have often

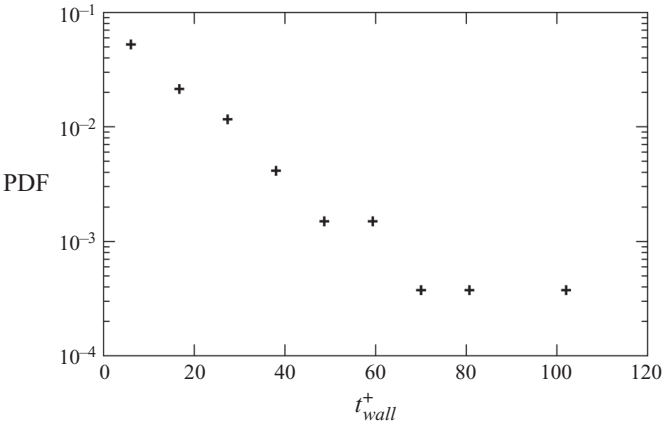

FIGURE 25. PDF of duration of particle–wall interactions, defined as the length of time particles spend continuously within 1.3 mean particle radii of the wall.

been modelled as induced by a random (Poissonian) distribution of turbulent fluctuations having sufficient strength to mobilize the particles (e.g. Papanicolaou *et al.* 2002). There are obvious differences between bedload transport and the present case: most notably, our particles are never at rest, as the wall shear stress exerted by the flow is much larger than the critical value for mobilizing them (Shields 1936). Still, our distribution of contact times suggests these can be modelled by a similar stochastic process driven by randomly occurring fluid flow events above a certain threshold. We note that Cameron, Nikora & Witz (2020) recently showed the importance of very-large-scale motions (non-random, spatially correlated turbulent events) for sediment entrainment. While this points to the limitations of considering turbulent fluctuations to be random, their study was conducted at much higher Reynolds numbers for which very-large-scale motions are more prominent than in our case (Smits, McKeon & Marusic 2011).

The exponential distribution of t_{wall} suggests a characteristic time τ_{wall}, such that its duration probability can be approximated as $\mathrm{PDF}(t_{wall}) \propto \exp(-t_{wall}/\tau_{wall})$. A least-squares fit returns $\tau_{wall} = 13.5\tau^+$, which is remarkably close to the particle response time $\tau_p/\tau^+ = St^+ = 15$. This suggests that both particle inertia and the fluid fluctuations play a role in determining the duration of the wall contact, and one may hypothesize a scaling $\tau^+_{wall} \sim St^+$. This is indeed consistent with the results reported by Ebrahimian *et al.* (2019), whose particles had $St^+ = 3.9$ and a mean wall contact time around $4\tau^+$. Because that is the only previous study reporting contact times for suspended particles, further research is warranted to corroborate this ansatz. We note that, in sediment transport, the waiting time was originally suggested by Einstein (1950) to be inversely proportional to the particle settling velocity, but it was later recognized that an inverse proportionality with fluid velocity showed better agreement with observations, and with the view that the particle entrainment rate depends on the strength of the turbulent fluctuations (Ancey *et al.* 2006, 2008).

As the particles are never at rest, one may consider the possibility that the short contact times are associated with a rebound process. However, even assuming an incident velocity V_i equal to the maximum vertical velocity in the $20\tau^+$ preceding touch-down (see below), the impact Stokes number $\rho_p V_i D_p/(9\mu)$ is of order unity – well below the threshold for a non-zero restitution coefficient (Joseph *et al.* 2001; Gondret, Lance & Petit 2002).

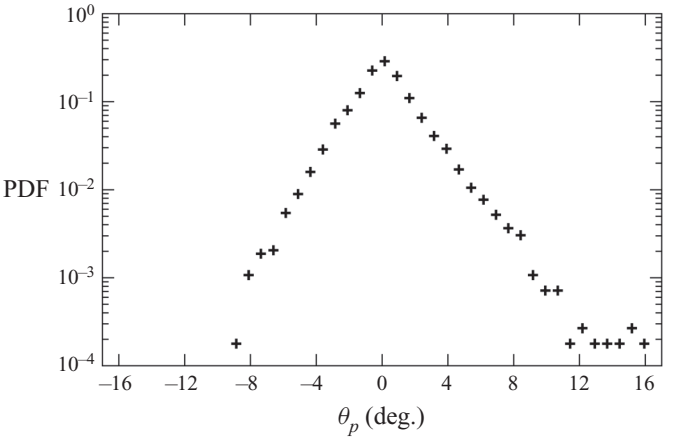

FIGURE 26. PDF of the angle of trajectories for near-wall ($y^+ < D_p^+$) particles.

Thus, in the present regime, the kinetic energy of the particle associated with its wall-normal motion is expected to be dissipated at contact, with no effective rebound.

The particle–wall interactions can also be characterized by the angle θ_p of near-wall particle trajectories as they approach or recede from the wall. The trajectory angle is defined as $\theta_p = \mathrm{atan}(v_p/u_p)$, such that θ_p is negative for particles approaching the wall and positive for particles receding from it. The set of particles within one particle diameter of the wall ($y^+ < 16$) is considered. The PDF of θ_p is shown in figure 26; it displays stretched tails (with a flatness of 6.7), and measurable preference for positive values (with a skewness of 0.65). The distribution of angles is narrower than what reported by Ebrahimian *et al.* (2019). This is attributed to the larger inertia of the present particles ($St^+ = 15$ versus 3.9), resulting in a slower response time to fluid velocity fluctuations and thus shallower near-wall trajectory angles. The positive skewness indicates that, despite gravity, relatively sharp lift-offs may occur.

The mechanisms behind particle touch-down and lift-off can be further understood by considering the Lagrangian averages along the particle trajectories. To this end, we first identify the moments of touch-down and lift-off (within the temporal resolution of $1/500$ s $= 0.7\tau^+$), and then average over all trajectories leading to and following those events, respectively. Figure 27 displays the average particle wall-normal distance, streamwise velocity and vertical velocity during the $20\tau^+$ before touch-down and after lift-off. We do not report Lagrangian statistics during particle–wall contact, as the range of contact durations thwarts a consistent averaging process. However, we note that the wall-normal positions, velocities and accelerations at touch-down are very close to those at lift-off.

The Lagrangian averages of the wall-normal distance indicate that the particles descending to the wall follow a somewhat steeper trajectory than those ascending from it (figures 27*a* and 27*b*). This is confirmed by the plots of the vertical velocities (figures 27*e* and 27*f*) and is due to a combination of gravity and Saffman lift (which is directed downward, as demonstrated below). The streamwise velocity declines before touch-down (figure 27*c*), because the particles approaching the wall are surrounded by slower and slower fluid, which applies on them drag in the negative x-direction. After lift-off, although the particles ascend at a similar pace as they descended, they regain streamwise velocity much more slowly (figure 27*d*). This fits the view of particles being lifted from

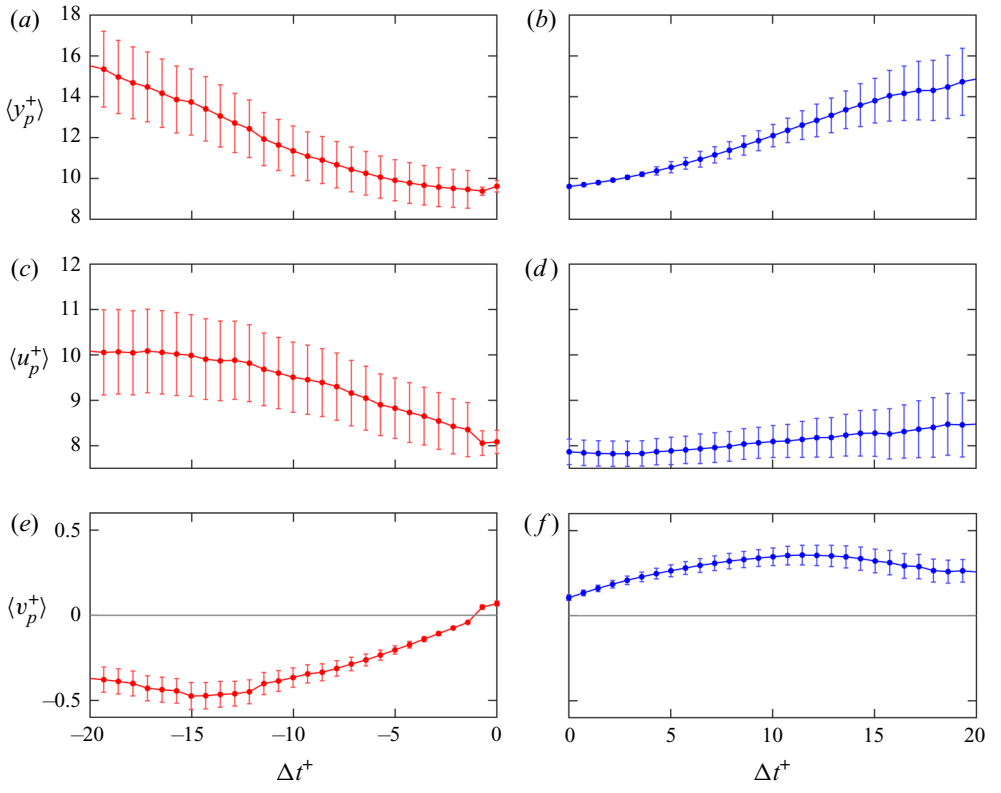

FIGURE 27. Lagrangian means of particle wall-normal coordinate (*a*,*b*), streamwise velocity (*c*,*d*) and wall-normal velocity (*e*,*f*) averaged over all identified touch-down events (*a*,*c*,*e*) and lift-off events (*b*,*d*,*f*). The time axis shows the time interval before or after lift-off or touch-down, respectively, and $\Delta t^+ = 0$ represents the moment of lift-off or touch-down.

the wall by ejections, i.e. events with smaller streamwise fluid momentum compared to the local mean.

The Lagrangian average of the fluid velocity experienced by the particles along their trajectory helps in the interpretation of the above trends. Figures 28(*a*) and 28(*b*) show that, before and after wall contact, the streamwise velocity of the fluid surrounding the particles is significantly lower than the local particle velocity (see figures 27*c* and 27*d*). (This is not captured by the unconditioned mean profiles presented §§ 3.1 and 3.2. We remark that the particles coming in contact with the wall are a small fraction of the total in the corresponding bin.) The direction of the streamwise slip velocity implies that, close to wall contact, drag acts against the direction of motion and Saffman lift is directed downward (in consideration of the slip velocity and the fluid velocity gradient, Saffman 1965). The streamwise fluid velocity along the trajectory is also significantly lower than the local mean fluid velocity (assuming a canonical boundary-layer profile, see figure 7); therefore, the particles are in regions of negative streamwise fluctuations. Because the vertical fluid velocity is negative before touch-down (figure 28*c*) and positive after lift-off (figure 28*d*), particles approaching and leaving the wall experience Q3 events and Q2 events, respectively. This confirms once more that ejections (in Q2) are critical to lift particles from the wall, while the role of sweeps (in Q4) is not dominant near wall contact. Importantly, figure 28(*d*) indicates that the vertical fluid velocity becomes positive just as the particles leave the wall: that is, lift-off happens when the particle starts to experience a

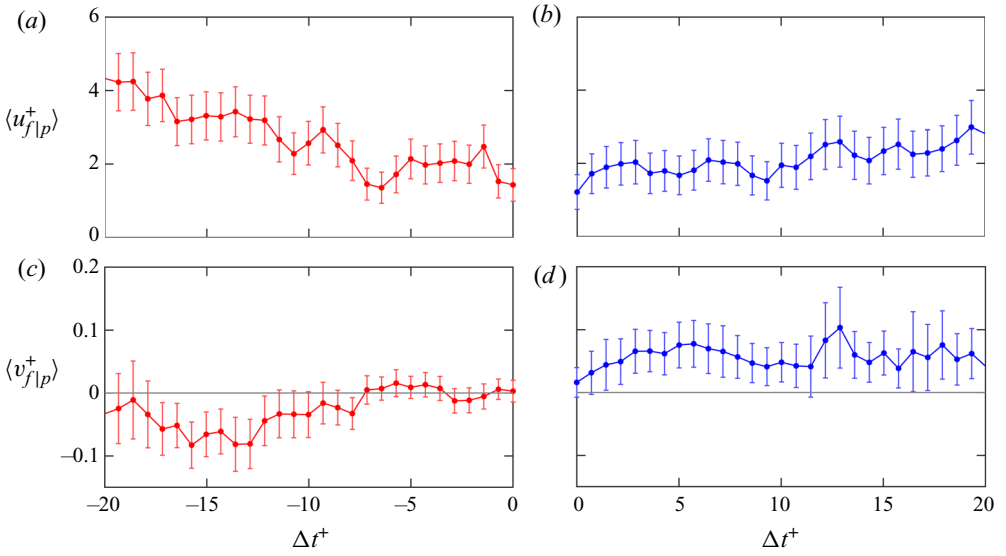

FIGURE 28. Lagrangian means of streamwise (*a*,*b*) and wall-normal (*c*,*d*) fluid velocity at particle location averaged over all identified touch-down events (*a*,*c*) and lift-off events (*b*,*d*). The time axis shows the time interval before or after lift-off or touch-down, respectively, and $\Delta t^+ = 0$ represents the moment of lift-off or touch-down.

fluid ejection. This is in line with the view that the duration of the contact time is dictated by the occurring of turbulent events.

A material frame of reference attached to the particles is the most appropriate to investigate the forces acting on them, and thus we now consider the accelerations tangential and normal to the local trajectory, $a_{t,p}$ and $a_{n,p}$, respectively

$$a_{t,p} = a_{x,p}\cos(\theta_p) + a_{y,p}\sin(\theta_p) \tag{3.7}$$

$$a_{n,p} = a_{y,p}\cos(\theta_p) - a_{x,p}\sin(\theta_p). \tag{3.8}$$

Note that since θ_p is relatively small, the tangential and normal accelerations are very similar in magnitude to the horizontal and vertical components, respectively. We can make inferences on the role and respective importance of drag, gravity and Saffman lift. Other forces are expected to be important as well, such as added mass, fluid acceleration, Basset history and Faxén corrections and rotation-induced (Magnus) lift (Maxey & Riley 1983; Crowe *et al.* 2011; Mathai *et al.* 2019); however, it is not trivial to infer their behaviour from experimental data, so our qualitative considerations will not focus on these forces.

The Lagrangian averages of the accelerations before and after wall contact are plotted in figure 29. As the particles approach the wall before touch-down, they experience increasingly negative tangential acceleration (figure 29*a*), reflecting the drag force opposing their motion. Notice that, while we are outside the assumptions of viscous steady flow made to derive analytical results, we expect the wall proximity to enhance drag for a particle moving parallel to a solid boundary (Brenner 1965). The negative streamwise acceleration peaks around $5\tau^+$ before touch-down and then decreases in magnitude. This is possibly due to lubrication effects, as the average particle is then only a fraction of its diameter away from the wall. Higher resolution measurements are needed to draw firm conclusions in this regard.

As the particles leave the wall and reach faster fluid layers, they at first experience negative streamwise acceleration, but this shrinks in magnitude and eventually reaches

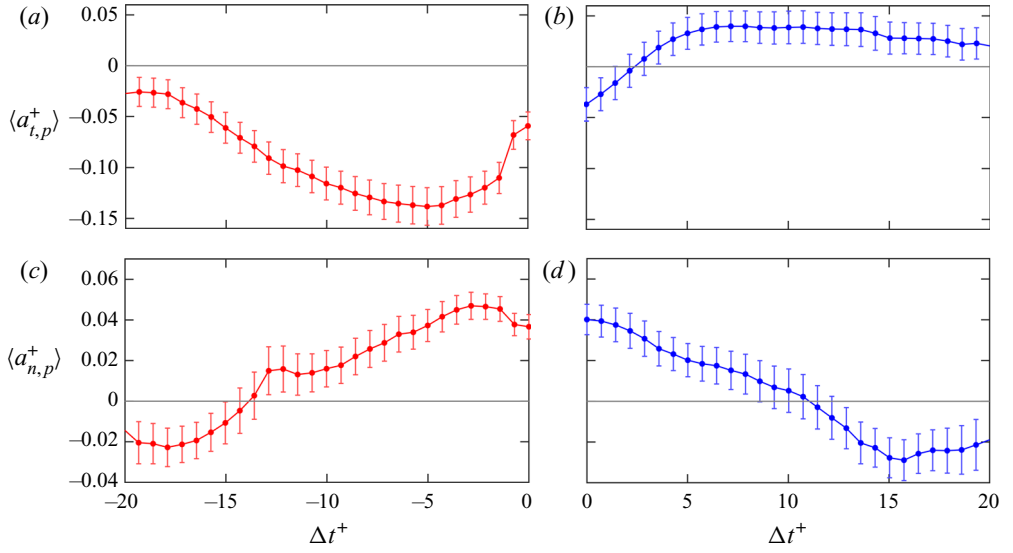

FIGURE 29. Lagrangian means of particle tangential acceleration (*a*,*b*) and normal acceleration (*c*,*d*) averaged over all identified touch-down events (*a*,*c*) and lift-off events (*b*,*d*). The time axis shows the time interval before or after lift-off or touch-down, respectively, and $\Delta t^+ = 0$ represents the moment of lift-off or touch-down.

a small positive plateau (figure 29*b*). This follows from the particles being entrained into faster fluid strata, which reduces the negative drag. However, because the particles are still faster than the surrounding fluid (see figures 27*d* and 28*b*), the drag is expected to remain negative. Thus, the positive streamwise acceleration must be a consequence of other forces. Added mass and fluid acceleration force are prime candidates, because the acceleration of the fluid along the particle trajectory is positive and larger than that of the particle (compare again figures 27*d* and 28*b*). Further studies to quantify these forces are warranted.

The normal acceleration becomes positive before touch-down (figure 29*c*) since the downward particle velocity is decreasing in magnitude as the wall is approached. This is qualitatively consistent with the increase in drag predicted in viscous flows when a particle travels towards a wall (Brenner 1965). The interaction with a lubrication layer may also contribute to slowing down the descent. The downward-directed Saffman lift increases the magnitude of the downward particle velocity before touch-down and decreases the magnitude of the upward velocity after lift-off. Thus, Saffman lift (along with gravity) is the likely cause of the drop in positive normal acceleration after the particles has left the wall (figure 29*d*). Simulations of Lee & Balachandar (2010) suggested the Magnus force to be relatively small, but the estimates of Ebrahimian *et al.* (2019) suggested it could be sufficient to overcome gravity. Here, the magnitude of the Magnus force cannot be estimated without knowing whether the particles are actually in contact with the wall, as this would dictate their rolling motion.

4. Conclusions

We have investigated the transport of inertial particles suspended in a turbulent boundary layer through simultaneous fluid and particle velocity measurements. While the considered regime is especially relevant to geophysical water flows, we have taken

a fundamental viewpoint and focused on the seemingly simple case of monodispersed spherical particles not depositing over the smooth wall. Leveraging the time-resolved, two-phase nature of the measurements, we documented in detail the particle–fluid dynamics and delved in several central aspects of this archetypical configuration. Given the richness of the flow physics, we chose to limit our attention to one specific regime, leaving parametric studies for the future.

We confirm that the particles travel at a lower mean velocity than the fluid, at least above the viscous sublayer. In the past, this has largely been attributed to the oversampling of slow velocity regions. While this is found to be the dominant factor in the logarithmic layer, closer to the wall the main cause for the mean velocity defect is the instantaneous particle slip from the surrounding fluid. Indeed, the expectation that particles would have a small instantaneous slip velocity is only tenable for small particle inertia and/or slow turbulence fluctuation, i.e. for small Stokes numbers. In the present regime ($St^+ = 15$), a significant portion of the fluid fluctuations experienced by the near-wall particles have shorter time scales than τ_p, and the inability of the particles to respond to them naturally translates in a sizeable slip velocity. By inspecting the profiles conditioned on ascending and descending particles, it appears that the mean velocity lag is due to the ascending ones, thus it is not directly related to gravity. The mean vertical velocity of the particles is close to the quiescent-fluid terminal velocity in the free stream, but it becomes vanishingly small approaching the wall. This is an effect of oversampling upward turbulent fluctuations, which is opposite to the behaviour in homogeneous turbulence.

The near-wall particle diffusivity in the streamwise direction is larger than the momentum eddy diffusivity, while the opposite is true in the wall-normal direction. This is one of the several instances in which the distinct (and competing) effects of gravity and inertia are on display. The dichotomy is highlighted here both by conditioning the statistics on ascending and descending particles, and by comparing outer and inner layers. This helps reconcile contrasting results in the literature and underscores the importance of both effects in realistic situations.

The near-wall particle transport is strongly linked to ejection events that promote resuspension, while the link with sweep events is weak. This suggests that turbophoresis, which is often considered a dominant feature according to studies where gravity is either absent or acting parallel to the wall, is at best a second-order effect when gravity is wall normal. Under equilibrium between settling and turbulent suspension, the concentration profile follows a power law with a much more gradual decrease from the wall than predicted by the Rouse–Prandtl theory (which neglects particle inertia), consistent with the observed reduction of settling velocity. While the particles in the inner layer do interact with the wall, the absence of bedload is reflected in the lack of a saltation layer in the mass flux profile.

Separating ascending and descending particles also helps us understand the root of the mean acceleration profile. Regions of positive and negative streamwise acceleration can be attributed to ascending and descending particles, respectively. Ascending particles find themselves surrounded by slower fluid which decelerates them (and more so because they are strongly associated with ejections); while descending particles are in the opposite condition, although this is due to gravity and not sweeps. By comparing with previous studies, we confirm that acceleration variance is larger for heavier particles, in stark contrast with the well-known trend in homogeneous turbulence. This is strictly a consequence of the crossing trajectories effect caused by gravitational drift, rather than by inertia. Indeed, near the wall, where the gravitational drift is smaller and the local St_η is larger, the accelerations are much less intermittent than further away from the wall.

Contrasting the effects of gravity and inertia is important to estimate the trends in different regimes. If the same particles are suspended in a turbulent boundary layer at higher Reynolds numbers, for example, the near-wall turbulence time scales will become smaller. Thus, the Stokes number (encapsulating the effect of inertia) will grow; while the friction velocity will increase, and so the Rouse number (representing the relative importance of gravitational drift) will shrink. Our conclusions then provide indications on the expected trends in such a case: the particles would lag the fluid more markedly; the settling rate would decrease; the particle Reynolds stresses would be even larger than the fluid's; the particle diffusivity would increase (the streamwise component becoming increasingly larger than the eddy diffusivity, and the vertical component getting closer to it); the concentration profile would get flatter; and the acceleration variance and intermittency would decrease. Future parametric studies are warranted to verify these predictions.

The duration of the wall–particle contact follows an exponential distribution, suggesting an analogy with the waiting times between deposition and entrainment in sediment transport: after touch-down, the particles slide along the wall (possibly over a lubrication layer we cannot resolve) until fluid fluctuations of sufficient strength lift them back into the stream. When expressed in wall units, the time scale of wall contact (i.e. the inverse of the entrainment rate) is close to St^+, in line with our interpretation of the process: a balance between particle inertia and fluid turbulence. The Lagrangian average along the trajectories before and after wall contact indicate that the particles descend more steeply towards the wall than they recede from it, due to a combination of gravity and Saffman lift. The latter is directed downward, because the particles in close proximity to the wall are faster than the fluid surrounding them. This also implies that the drag force opposes the particle streamwise motion. The impact velocity is well below the threshold for significant energy restitution, therefore there is effectively no rebound. The lift-off coincides with the particles meeting a fluid ejection, reaffirming the importance of these events in the particle transport. The particles accelerate after leaving the wall, even while they are still faster than the surrounding fluid; this is likely an effect of added mass and fluid acceleration forces. Future experiments focused on the near-wall region with higher resolution and the ability to detect particle rotation are needed to determine the fluid velocity gradients surrounding the particles and assess the role of lubrication forces and rotation-induced lift.

Different configurations (e.g. particles of different size and density) will display different behaviours. In particular, the particle size is expected to have an important impact on the near-wall behaviour, where the velocity gradients are sharper. The present results, however, paint a coherent picture of the multi-faceted problem, shed some new light on a series of long-standing issues, and isolate new questions that require an even deeper investigation. Moreover, inasmuch as we reported novel statistics for several previously undocumented quantities, the results should be useful for developing and validating numerical models.

Acknowledgements

This work was funded by the Legislative-Citizen Commission on Minnesota Resources (LCCMR). L.J.B. was supported by the Department of Defense (DoD) through the National Defense Science & Engineering Graduate Fellowship (NDSEGF) Program.

Declaration of interests

The authors report no conflict of interest.

REFERENCES

ADHIKARI, D. 2013 Volumetric velocity measurement of aquatic predator-prey interactions. PhD thesis, University of Minnesota.

ANCEY, C., BÖHM, T., JODEAU, M. & FREY, P. 2006 Statistical description of sediment transport experiments. *Phys. Rev.* E **74** (1), 011302.

ANCEY, C., DAVISON, A. C., BÖHM, T., JODEAU, M. & FREY, P. 2008 Entrainment and motion of coarse particles in a shallow water stream down a steep slope. *J. Fluid Mech.* **595**, 83–114.

AYYALASOMAYAJULA, S., GYLFASON, A., COLLINS, L. R., BODENSCHATZ, E. & WARHAFT, Z. 2006 Lagrangian measurements of inertial particle accelerations in grid generated wind tunnel turbulence. *Phys. Rev. Lett.* **97** (14), 144507.

BAGNOLD, R. A. 1936 The movement of desert sand. *Proc. R. Soc. Lond.* A **157** (892), 594–620.

BAGNOLD, R. A. 1941 *The Physics of Blown Sand and Desert Dunes*. Methuen.

BAKER, L. J. & COLETTI, F. 2019 Experimental study of negatively buoyant finite-size particles in a turbulent boundary layer up to dense regimes. *J. Fluid Mech.* **866**, 598–629.

BALACHANDAR, S., LIU, K. & LAKHOTE, M. 2019 Self-induced velocity correction for improved drag estimation in Euler–Lagrange point-particle simulations. *J. Comput. Phys.* **376**, 160–185.

BEC, J., BIFERALE, L., BOFFETTA, G., CELANI, A., CENCINI, M., LANOTTE, A., MUSACCHIO, S. & TOSCHI, F. 2006 Acceleration statistics of heavy particles in turbulence. *J. Fluid Mech.* **550**, 349–358.

BENDAT, J. S. & PIERSOL, A. G. 2011 *Random Data: Analysis and Measurement Procedures*, vol. 729. John Wiley & Sons.

BERK, T. & COLETTI, F. 2020 Transport of inertial particles in high-Reynolds-number turbulent boundary layers. *J. Fluid Mech.* **903**, A18.

BERNARDINI, M. 2014 Reynolds number scaling of inertial particle statistics in turbulent channel flows. *J. Fluid Mech.* **758**, R1.

BRENNER, H. 1965 Effect of finite boundaries on the Stokes resistance of an arbitrary particle. *J. Fluid Mech.* **12** (1), 35–48.

CAMERON, S. M., NIKORA, V. I. & WITZ, M. J. 2020 Entrainment of sediment particles by very large-scale motions. *J. Fluid Mech.* **888**, A7.

CAPECELATRO, J. & DESJARDINS, O. 2013 An Euler–Lagrange strategy for simulating particle-laden flows. *J. Comput. Phys.* **238**, 1–31.

CHOI, J.-I., YEO, K. & LEE, C. 2004 Lagrangian statistics in turbulent channel flow. *Phys. Fluids* **16** (3), 779–793.

CLIFT, R., GRACE, J. R. & WEBER, M. E. 2005 *Bubbles, Drops, and Particles*. Dover Publications.

CROWE, C. T., SCHWARZKOPF, J. D., SOMMERFELD, M. & TSUJI, Y. 2011 *Multiphase Flows with Droplets and Particles*. CRC Press.

CSANADY, G. T. 1963 Turbulent diffusion of heavy particles in the atmosphere. *J. Atmos. Sci.* **20** (3), 201–208.

DE GRAAFF, D. B. & EATON, J. K. 2000 Reynolds-number scaling of the flat-plate turbulent boundary layer. *J. Fluid Mech.* **422**, 319–346.

EBRAHIMIAN, M., SANDERS, R. S. & GHAEMI, S. 2019 Dynamics and wall collision of inertial particles in a solid–liquid turbulent channel flow. *J. Fluid Mech.* **881**, 872–905.

EINSTEIN, H. A. 1950 *The Bed-Load Function for Sediment Transportation in Open Channel Flows*. US Government Printing Office.

ELGHOBASHI, S. & TRUESDELL, G. C. 1992 Direct simulation of particle dispersion in a decaying isotropic turbulence. *J. Fluid Mech.* **242**, 655–700.

FAN, N., SINGH, A., GUALA, M., FOUFOULA-GEORGIOU, E. & WU, B. 2016 Exploring a semimechanistic episodic Langevin model for bed load transport: emergence of normal and anomalous advection and diffusion regimes. *Water Resour. Res.* **52** (4), 2789–2801.

FONG, K. O., AMILI, O. & COLETTI, F. 2019 Velocity and spatial distribution of inertial particles in a turbulent channel flow. *J. Fluid Mech.* **872**, 367–406.

GERASHCHENKO, S., SHARP, N. S., NEUSCAMMAN, S. & WARHAFT, Z. 2008 Lagrangian measurements of inertial particle accelerations in a turbulent boundary layer. *J. Fluid Mech.* **617**, 255–281.

GONDRET, P., LANCE, M. & PETIT, L. 2002 Bouncing motion of spherical particles in fluids. *Phys. Fluids* **14** (2), 643–652.

GUALA, M., MANES, C., CLIFTON, A. & LEHNING, M. 2008 On the saltation of fresh snow in a wind tunnel: profile characterization and single particle statistics. *J. Geophys. Res.: Earth* **113**, F03024.

GUALTIERI, P., PICANO, F., SARDINA, G. & CASCIOLA, C. M. 2015 Exact regularized point particle method for multiphase flows in the two-way coupling regime. *J. Fluid Mech.* **773**, 520–561.

HEYMAN, J., BOHORQUEZ, P. & ANCEY, C. 2016 Entrainment, motion, and deposition of coarse particles transported by water over a sloping mobile bed. *J. Geophys. Res.: Earth* **121** (10), 1931–1952.

HORWITZ, J. A. K. & MANI, A. 2016 Accurate calculation of Stokes drag for point–particle tracking in two-way coupled flows. *J. Comput. Phys.* **318**, 85–109.

VAN HOUT, R. 2011 Time-resolved PIV measurements of the interaction of polystyrene beads with near-wall-coherent structures in a turbulent channel flow. *Intl J. Multiphase Flow* **37** (4), 346–357.

VAN HOUT, R. 2013 Spatially and temporally resolved measurements of bead resuspension and saltation in a turbulent water channel flow. *J. Fluid Mech.* **715**, 389.

VAN HOUT, R., SABBAN, L. & COHEN, A. 2013 The use of high-speed PIV and holographic cinematography in the study of fiber suspension flows. *Acta Mechanica* **224** (10), 2263–2280.

HURTHER, D. & LEMMIN, U. 2003 Turbulent particle flux and momentum flux statistics in suspension flow. *Water Resour. Res.* **39** (5), 1139.

IRELAND, P. J. & DESJARDINS, O. 2017 Improving particle drag predictions in Euler–Lagrange simulations with two-way coupling. *J. Comput. Phys.* **338**, 405–430.

JOSEPH, G. G., ZENIT, R., HUNT, M. L. & ROSENWINKEL, A. M. 2001 Particle–wall collisions in a viscous fluid. *J. Fluid Mech.* **433**, 329–346.

JUNG, J., YEO, K. & LEE, C. 2008 Behavior of heavy particles in isotropic turbulence. *Phys. Rev.* E **77** (1), 016307.

KAFTORI, D., HETSRONI, G. & BANERJEE, S. 1995*a* Particle behavior in the turbulent boundary layer. I. Motion, deposition, and entrainment. *Phys. Fluids* **7** (5), 1095–1106.

KAFTORI, D., HETSRONI, G. & BANERJEE, S. 1995*b* Particle behavior in the turbulent boundary layer. II. Velocity and distribution profiles. *Phys. Fluids* **7** (5), 1107–1121.

KIDANEMARIAM, A. G., CHAN-BRAUN, C., DOYCHEV, T. & UHLMANN, M. 2013 Direct numerical simulation of horizontal open channel flow with finite-size, heavy particles at low solid volume fraction. *New J. Phys.* **15** (2), 025031.

KIGER, K. T. & PAN, C. 2002 Suspension and turbulence modification effects of solid particulates on a horizontal turbulent channel flow. *J. Turbul.* **3** (19), 1–17.

KOK, J. F., PARTELI, E. J. R., MICHAELS, T. I. & KARAM, D. B. 2012 The physics of wind-blown sand and dust. *Rep. Prog. Phys.* **75** (10), 106901.

LAJEUNESSE, E., MALVERTI, L. & CHARRU, F. 2010 Bed load transport in turbulent flow at the grain scale: experiments and modeling. *J. Geophys. Res.: Earth* **115**, F04001.

LAVEZZO, V., SOLDATI, A., GERASHCHENKO, S., WARHAFT, Z. & COLLINS, L. R. 2010 On the role of gravity and shear on inertial particle accelerations in near-wall turbulence. *J. Fluid Mech.* **658**, 229–246.

LEE, H. & BALACHANDAR, S. 2010 Drag and lift forces on a spherical particle moving on a wall in a shear flow at finite Re. *J. Fluid Mech.* **657**, 89–125.

LEE, J. & LEE, C. 2015 Modification of particle-laden near-wall turbulence: effect of Stokes number. *Phys. Fluids* **27** (2), 023303.

LEE, J. & LEE, C. 2019 The effect of wall-normal gravity on particle-laden near-wall turbulence. *J. Fluid Mech.* **873**, 475–507.

LI, J., WANG, H., LIU, Z., CHEN, S. & ZHENG, C. 2012 An experimental study on turbulence modification in the near-wall boundary layer of a dilute gas-particle channel flow. *Exp. Fluids* **53** (5), 1385–1403.

LIN, Z.-W., SHAO, X.-M., YU, Z.-S. & WANG, L.-P. 2017 Effects of finite-size heavy particles on the turbulent flows in a square duct. *J. Hydrodyn.* **29** (2), 272–282.

MARCHIOLI, C. 2017 Large-eddy simulation of turbulent dispersed flows: a review of modelling approaches. *Acta Mechanica* **228** (3), 741–771.

MARCHIOLI, C. & SOLDATI, A. 2002 Mechanisms for particle transfer and segregation in a turbulent boundary layer. *J. Fluid Mech.* **468**, 283–315.

MATHAI, V., LOEFFEN, L. A. W. M., CHAN, T. T. K. & WILDEMAN, S. 2019 Dynamics of heavy and buoyant underwater pendulums. *J. Fluid Mech.* **862**, 348–363.

MAXEY, M. R. & RILEY, J. J. 1983 Equation of motion for a small rigid sphere in a nonuniform flow. *Phys. Fluids* **26** (4), 883–889.

MORDANT, N., CRAWFORD, A. M. & BODENSCHATZ, E. 2004 Experimental Lagrangian acceleration probability density function measurement. *Physica* D **193** (1-4), 245–251.

NEMES, A., DASARI, T., HONG, J., GUALA, M. & COLETTI, F. 2017 Snowflakes in the atmospheric surface layer: observation of particle–turbulence dynamics. *J. Fluid Mech.* **814**, 592–613.

NIELSEN, P. 1993 Turbulence effects on the settling of suspended particles. *J. Sedim. Res.* **63** (5), 835–838.

NIÑO, Y. & GARCIA, M. H. 1996 Experiments on particle–turbulence interactions in the near-wall region of an open channel flow: implications for sediment transport. *J. Fluid Mech.* **326**, 285–319.

NISHIMURA, K. & HUNT, J. C. R. 2000 Saltation and incipient suspension above a flat particle bed below a turbulent boundary layer. *J. Fluid Mech.* **417**, 77–102.

PAPANICOLAOU, A. N., DIPLAS, P., EVAGGELOPOULOS, N. & FOTOPOULOS, S. 2002 Stochastic incipient motion criterion for spheres under various bed packing conditions. *J. Hydraul. Engng ASCE* **128** (4), 369–380.

PETERSEN, A. J., BAKER, L. & COLETTI, F. 2019 Experimental study of inertial particles clustering and settling in homogeneous turbulence. *J. Fluid Mech.* **864**, 925–970.

PICANO, F., BREUGEM, W.-P. & BRANDT, L. 2015 Turbulent channel flow of dense suspensions of neutrally buoyant spheres. *J. Fluid Mech.* **764**, 463–487.

POPE, S. B. 2000 *Turbulent Flows*. Cambridge University Press.

PRANDTL, L. 1952 *Essentials of Fluid Dynamics: with Applications to Hydraulics, Aeronautics, Meteorology and Other Subjects*. Hafner Publishing Company.

RABENCOV, B., ARCA, J. & VAN HOUT, R. 2014 Measurement of polystyrene beads suspended in a turbulent square channel flow: spatial distributions of velocity and number density. *Intl J. Multiphase Flow* **62**, 110–122.

REEKS, M. W. 1977 On the dispersion of small particles suspended in an isotropic turbulent fluid. *J. Fluid Mech.* **83** (3), 529–546.

RICHTER, D. H. & SULLIVAN, P. P. 2014 Modification of near-wall coherent structures by inertial particles. *Phys. Fluids* **26** (10), 103304.

RIGHETTI, M. & ROMANO, G. P. 2004 Particle–fluid interactions in a plane near-wall turbulent flow. *J. Fluid Mech.* **505**, 93–121.

RIMON, Y. & CHENG, S. I. 1969 Numerical solution of a uniform flow over a sphere at intermediate Reynolds numbers. *Phys. Fluids* **12** (5), 949–959.

ROBINSON, S. K. 1991 Coherent motions in the turbulent boundary layer. *Annu. Rev. Fluid Mech.* **23** (1), 601–639.

ROUSE, H. 1937 Modern conceptions of the mechanics of fluid turbulence. *Trans. Am. Soc. Civ. Engng* **102**, 463–505.

ROUSON, D. W. I. & EATON, J. K. 2001 On the preferential concentration of solid particles in turbulent channel flow. *J. Fluid Mech.* **428**, 149–169.

SABBAN, L. & VAN HOUT, R. 2011 Measurements of pollen grain dispersal in still air and stationary, near homogeneous, isotropic turbulence. *J. Aerosol Sci.* **42** (12), 867–882.

SAFFMAN, P. G. T. 1965 The lift on a small sphere in a slow shear flow. *J. Fluid Mech.* **22** (2), 385–400.

SARDINA, G., SCHLATTER, P., BRANDT, L., PICANO, F. & CASCIOLA, C. M. 2012 Wall accumulation and spatial localization in particle-laden wall flows. *J. Fluid Mech.* **699**, 50–78.

SHIELDS, A. 1936 Anwendung der Aehnlichkeitsmechanik und der Turbulenzforschung auf die Geschiebebewegung. PhD thesis, Technical University Berlin.

SMITS, A. J., MCKEON, B. J. & MARUSIC, I. 2011 High–Reynolds number wall turbulence. *Annu. Rev. Fluid Mech.* **43**, 353–375.

SQUIRES, K. D. & EATON, J. K. 1991 Measurements of particle dispersion obtained from direct numerical simulations of isotropic turbulence. *J. Fluid Mech.* **226**, 1–35.

TANIÈRE, ANNE & ARCEN, BORIS 2016 Overview of existing Langevin models formalism for heavy particle dispersion in a turbulent channel flow. *Intl J. Multiphase Flow* **82**, 106–118.

TANIÈRE, A., OESTERLÉ, B. & MONNIER, J. C. 1997 On the behaviour of solid particles in a horizontal boundary layer with turbulence and saltation effects. *Exp. Fluids* **23** (6), 463–471.

TAYLOR, G. I. 1921 Diffusion by continuous movements. *Proc. Lond. Math. Soc.* **s2-20** (1), 196–212.

TEE, Y. H., BARROS, D. & LONGMIRE, E. K. 2020 Motion of finite-size spheres released in a turbulent boundary layer. *Intl J. Multiphase Flow* **133**, 103462.

VOTH, G. A., LA PORTA, A., CRAWFORD, A. M., ALEXANDER, J. & BODENSCHATZ, E. 2002 Measurement of particle accelerations in fully developed turbulence. *J. Fluid Mech.* **469**, 121–160.

WANG, G., ABBAS, M. & CLIMENT, É. 2017 Modulation of large-scale structures by neutrally buoyant and inertial finite-size particles in turbulent Couette flow. *Phys. Rev. Fluids* **2** (8), 084302.

WANG, G., FONG, K. O., COLETTI, F., CAPECELATRO, J. & RICHTER, D. H. 2019 Inertial particle velocity and distribution in vertical turbulent channel flow: a numerical and experimental comparison. *Intl J. Multiphase Flow* **120**, 103105.

WANG, L.-P. & MAXEY, M. R. 1993 Settling velocity and concentration distribution of heavy particles in homogeneous isotropic turbulence. *J. Fluid Mech.* **256**, 27–68.

WANG, L.-P. & STOCK, D. E. 1993 Dispersion of heavy particles by turbulent motion. *J. Atmos. Sci.* **50** (13), 1897–1913.

WELLS, M. R. & STOCK, D. E. 1983 The effects of crossing trajectories on the dispersion of particles in a turbulent flow. *J. Fluid Mech.* **136**, 31–62.

WESTERWEEL, J. & SCARANO, F. 2005 Universal outlier detection for PIV data. *Exp. Fluids* **39**, 1096–1100.

ZAMANSKY, R., VINKOVIC, I. & GOROKHOVSKI, M. 2011 Acceleration statistics of solid particles in turbulent channel flow. *Phys. Fluids* **23** (11), 113304.

ZHAO, L. H., ANDERSSON, H. I. & GILLISSEN, J. J. J. 2010 Turbulence modulation and drag reduction by spherical particles. *Phys. Fluids* **22** (8), 081702.

ZHU, H.-Y., PAN, C., WANG, J.-J., LIANG, Y.-R. & JI, X.-C. 2019 Sand-turbulence interaction in a high-Reynolds-number turbulent boundary layer under net sedimentation conditions. *Intl J. Multiphase Flow* **119**, 56–71.